Abstract of "Computational Studies of Fracture in Micro- and Nano-Scale Structures" by Rassin Grantab, Ph.D., Brown University, May 2012.

The electronics industry drives a great deal of research towards inventing methods for creating smaller devices. In order for the current trend of the diminishing size of electronic devices - such as cell phones and laptops - to continue, two main breakthroughs are necessary: firstly, the electronic components themselves must become smaller without a loss of computing power; and secondly, the batteries that store the energy for these devices must also become smaller without a loss of capacity. Semiconductor nanowires and graphene present promising solutions for making smaller electronic circuits, while lithium-ion batteries are currently the most space-efficient energy-storage device. In order for nanowires, graphene, and lithium-ion batteries to gain widespread use, both their performance and reliability are of paramount importance. Despite the fact that these nano- and micro-scale structures are not directly under mechanical loads, their reliability is still largely dictated by mechanical failure during use, and therefore must be well-understood. To this end, the work presented herein describes detailed analyses of fracture and failure in these small-scale structures. At the nano-scale, fracture in faceted semiconductor nanowires and graphene sheets containing grain boundaries has been studied using molecular dynamics techniques. Interestingly, the results of the molecular dynamics simulations of the nanowires can easily be explained using continuum fracture mechanics, while the results of the graphene sheets with grain boundaries are in complete discord with continuum theories and general intuition. In the case of the lithium-ion batteries, finite element simulations of crack propagation in electrodes have been used to understand how initial defects grow in graphite and silicon electrode particles during battery charging and use.

Computational Studies of Fracture in Micro- and Nano-Scale Structures

by

Rassin Grantab

Sc.M., Applied Mathematics, Brown University, 2010

M.A.Sc., Mechanical Engineering, University of Waterloo, 2006

B.A.Sc., Mechanical Engineering, University of Waterloo, 2004

A dissertation submitted in partial fulfillment of the
requirements for the Degree of Doctor of Philosophy
in the School of Engineering at Brown University

Providence, Rhode Island

May 2012

This dissertation by Rassin Grantab is accepted in its present form by the School of Engineering as satisfying the dissertation requirement for the degree of Doctor of Philosophy.

Date _____ _____

Professor Vivek B. Shenoy, Advisor

Recommended to the Graduate Council

Date _____ _____

Professor Pradeep R. Guduru, Reader

Date _____ _____

Professor Brian W. Sheldon, Reader

Approved by the Graduate Council

Date _____ _____

Professor Peter M. Weber
Dean of the Graduate School

Vita

Rassin Grantab was born on October 23, 1980 in Tehran, Iran, and immigrated to Toronto, Canada, in June 1989. He began his bachelor's studies in Mechanical Engineering at the University of Waterloo in 1999, and received his degree in April, 2004. Upon graduation, he pursued a master's degree in Mechanical Engineering at the same institution, completing that degree in August, 2006. He then joined the Solid Mechanics program at Brown University, and en route to his Ph.D., he received a masters degree in Applied Mathematics in May 2010.

Acknowledgements

Firstly, I would like to thank my advisor, Prof. Vivek Shenoy, for providing me with the opportunity to work on a variety of interesting mechanics projects. He has entrusted me with dictating the direction of projects and given me a level of academic freedom that few graduate students enjoy. I would like to express my gratitude to my thesis readers, Prof. Pradeep Guduru and Prof. Brian Sheldon, for taking the time to review and comment on my research work. I would also like to thank Prof. Ben Freund for kindly helping me many times over the past 5 years.

I owe many thanks to my colleagues that have helped me along the way, most notably, Eric Buchovecky, Nikhil Medhekar, Julie Waters, Asha Nurse, David Cipoletti, Yi Dong, Akbar Bagri, Peng Chen, and Maria Stournara. My time at Brown would certainly have been very dull and unfulfilling had it not been for my great friends, and so I must thank Avram Levi, Dhiraj Catoor, Padam Jain, Batur Ercan, Gavril Gavrilovich, Jim Rice, Indrek Külaots, Jessica Jalbert, Tatiana Vasilieva, Anil Usumezbas, Osman Ulusoy, Ashi Ranjan, Sabrina Puckett, Gerry Della Rocca, and Neil Rajan.

My parents and sister have always been very supportive of me and for that I am always grateful. Last and absolutely-not-least, I must thank Silja, without whom I never would have finished.

Für Silja

Contents

⋆ Parts of this thesis have appeared in the following peer-reviewed publications:

Grantab, R. and Shenoy, V. B. (2011), 'Location- and Orientation-Dependent Progressive Crack Propagation in Cylindrical Graphite Electrode Particles', *Journal of the Electrochemical Society* **158**(8), A948–A954.

Grantab, R. and Shenoy, V. B. (2011), 'The Key Role of Nanoscale Surface Facets on the Mechanical Strength and Failure of Wurtzite and Periodically Twinned Zinc-Blende Nanowires', *Philosophical Magazine Letters* **91**(4), 280–286.

Grantab, R., Shenoy, V. B. and Ruoff, R.S. (2010), 'Anomalous Strength Characteristics of Tilt Grain Boundaries in Graphene', *Science* **330**(6006), 946–948.

List of Tables

List of Figures

Chapter 1

Introduction and Overview

Looking back at the history of computers starting with the very first machines of the mid-20th century, the reduction in size to that of modern-day computers and laptops is startling. The size differences are even more incredible when one considers that they were concurrent with equally impressive increases in computing power. The very first computers of the 1950s utilized vacuum tubes, but by the 1960s, these had been replaced by transistors, which provided the first major decrease in size and increase in power. Another major step came in the 1970s with the advent of integrated circuits which ultimately led to the invention of the microprocessor, a technology still in widespread use today [Lavington (1998)]. From the very beginning, each drastic decrease in size and increase in computing power was made possible by a completely new technology as the basis for the electronic elements. Small incremental improvements to microprocessors are ongoing, however, in order for the trend of major decreases in size and increases in performance to continue, a new technology must supersede microprocessors.

Two promising technologies - nanowires and graphene - have emerged in recent years that may allow this evolution to continue. Semiconductor nanowires have been developed by a number of research groups [Dick et al. (2004), Algra et al. (2008),

Caroff et al. (2009), Ross (2009)], and their use in electronics has been demonstrated in devices such as memory storage units [Thelander et al. (2005)]. One class of semiconductor nanowires possessing excellent electronic properties are comprised of a pair of materials from the III and V group of the periodic table, usually referred to simply as III-V nanowires. Depending on the growth conditions, these nanowires can have different types of surface facets and electronic properties.

Graphene has garnered a great deal of attention since it is the thinnest material ever synthesized (it is only 1 atom thick) yet one of the strongest (roughly $100GPa$ strength at failure) and stiffest (roughly $1TPa$ modulus) ever measured [Lee et al. (2008)]. Due to its optical and electronic properties, it is also a very promising material for use in future computing devices [Geim (2009)]. The main challenge with graphene lies in producing large area single layer sheets, which is currently a widely-researched area in physics and materials science.

Nanowires and graphene may eventually lead to significant decreases in the size of computers, but the pervasiveness of portable electronics has created another important requirement: reliable and space-efficient energy storage. In order to reduce the overall size of portable electronics, both the computing components and energy storage devices must be made smaller and more efficient. Currently, lithium-ion batteries have the highest specific capacity of all known battery chemistries [Aifantis et al. (2007)], and a great deal of research is concerned with improving the capacity of these batteries.

Besides simply developing such technologies and putting them to practical use, it is important to ensure the reliability of the devices utilizing them. Although the aforementioned technologies will not be placed under direct mechanical loading in electronic devices, they can nevertheless fracture during manufacturing, or fail due

to stresses that are generated by other means during use. In the case of III-V semiconductor nanowires, their surface facets may influence their strength and lead to difficulties during manufacturing, therefore the role of surface facets on the mechanical strength of the nanowires must be understood. New graphene synthesis techniques are able to produce larger areas of single-layer graphene, however, the resulting sheets contain grain boundaries [Li et al. (2009)]; in order to make use of graphene synthesized in this manner, the effects of the grain boundaries on the mechanical strength of graphene should be well-studied. During use, the electrodes of lithium-ion batteries undergo volumetric expansion during lithium intercalation which leads to stresses; if the stresses are sufficiently high, fracture ensues and causes the capacity of the batteries to deteriorate over time. It is for this reason that understanding crack propagation in lithium-ion battery electrodes is an important endeavor for the scientific community.

In this thesis, we present computational studies of fracture in the aforementioned technologies. In the first half, we use molecular dynamics simulations to study the nano-scale failure of semiconductor nanowires (Chapter 2) and graphene (Chapter 3). The latter half of the thesis uses finite element simulations to investigate crack propagation in graphite (Chapter 4) and silicon (Chapter 5) electrode particles used in lithium-ion batteries.

This thesis is organized in such a way that the introductory sections of each chapter will provide the reader with sufficient background information, and references to the literature. Therefore, in order to avoid redundancy, additional remarks of an introductory nature for each specific topic have been omitted in this section.

Chapter 2

Fracture of III-V Semiconductor Nanowires

2.1 Introduction

Semiconductor nanowires have attracted a great deal of attention recently, mainly due to their potential applications in electronics, photonics, electromechanical systems, and life sciences [Johansson et al. (2006), Joyce et al. (2007), Patolsky et al. (2006)]. Several devices comprised of nanowires have already been demonstrated, such as nanowire lasers [Huang et al. (2001), Duan et al. (2003)], photodetectors [Pettersson et al. (2006)], field-effect transistors [Ng et al. (2004)], single-electron memory devices [Thelander et al. (2005)], and biosensors [Patolsky et al. (2006)]. The electronic properties of nanowires can be controlled by changing their size and shape, as well as introducing defects such as twins. For example, the introduction of periodic twins can lead to a direct band gap in indirect band gap materials such as Si, SiC, and GaP [Ross (2009), Algra et al. (2008)]. Recently, Caroff et al. (2009) and Algra et al. (2008) have developed a method to grow periodically-twinned $< 111 >$-oriented III-V

nanowires consisting of a Zinc-Blende (ZB) crystal structure in a manner that allows control over the spacing between the twins. In addition to the periodically-twinned wires, twin-free III-V nanowires consisting of a Wurtzite (WZ) crystal structure have been grown by Dick et al. (2004).

While periodically-twinned superlattices have received attention for their electronic properties, they can also provide crucial insights into how defects and imperfections influence failure mechanisms at the nanoscale. A key issue that is of interest is to identify means by which defect and surface morphology can be used to control not only electronic, but mechanical properties. It is particularly relevant to understand how periodic twins and surface facets affect strength and ductility at the nanoscale. The role of surface facets on the mechanical properties of metallic nanowires (eg. gold [Deng and Sansoz (2009)] and copper [Zhang and Huang (2009)]) have been investigated using molecular dynamics simulations. It has been observed that surface facets lower the stress required to nucleate dislocations during deformation [Zhang and Huang (2009)]. Since twin boundaries impede dislocation cross-slip, the higher dislocation density of the faceted nanowires makes them stronger than non-faceted (i.e., circular cross-section) nanowires [Zhang and Huang (2009)]. Distinct surface facets are also observed in III-V semiconductor nanowires in both WZ and ZB form; the periodically-twinned ZB nanowires have {111} type surface-facets that alternate their orientations at each twin-plane, while the twin-free WZ nanowires have $\{11\overline{2}\}$ type surface facets.

The mechanical properties of semiconductor nanowires made of silicon [Kang and Cai (2007)], germanium [Kang and Cai (2007)], zinc-oxide [Wen et al. (2008)], and silicon-carbide [Makeev et al. (2006)] (although not a III-V material, silicon-carbide has been observed as both ZB [Zhang, Shim and Huang (2008)] and WZ [Makeev et al. (2006)]), have also been investigated through simulations. Very recently, Zhu et al.

(2009) have experimentally measured the mechanical properties of vapor-liquid-solid synthesized silicon nanowires and found that the elastic modulus of the nanowires decreased while the fracture strength increased as the nanowire radius was reduced.

Based on the conclusions drawn from work on metallic nanowires that are ductile [Zhang and Huang (2009)], it is expected that surface facets can have an effect on the brittle failure of semiconductor nanowires, but to what extent? How does the shape of a III-V nanowire influence its mechanical properties? Can certain shapes and surface facets lead to stronger nanowires? How do periodic twins affect the deformation behavior of nanowires? The aim of this chapter is to address these questions and understand the effects of the innate surface facets of III-V nanowires on their behavior during tensile deformation. We present molecular dynamics results for three different material systems - GaAs, InAs, and SiC - which allow us to make very general conclusions pertaining to the role of surface facets and shapes of nanowires on the brittle failure of a large class of compound semiconductor nanowires. In particular, we have found that the surface facets inherent to WZ nanowires provide an energetically favorable site for crack nucleation when compared to non-faceted wires. We have also concluded that the surface facets found on ZB nanowires lead to stress singularities that make them more prone to failure than WZ nanowires.

2.2 Computational Methods

Molecular dynamics (MD) simulations were performed on [111] oriented WZ and ZB nanowires using the parallel MD package, LAMMPS [Plimpton (1995)]. We considered nanowires ranging in length from $150 - 210$Å, and ensured that our results were not influenced by finite size effects. An ancillary study was performed in order to choose an appropriate radius for the nanowires and it was observed that the results did not change appreciably as the nanowire radius exceeded 50Å (refer to Figure

2.3(a) for the definition of nanowire radius), therefore this value was used for all the nanowires in our study (an average radius of 50Å was used for the ZB nanowires). We have omitted a detailed overview of these relatively minor size-effects in order to focus our attention on the effects of surface facets on the mechanical behavior of the nanowires. In the case of the ZB nanowires, the ratio of twin-plane spacing to nanowire diameter was chosen such that the overall geometry reflected that of experimentally grown ZB nanowires [Caroff et al. (2009)].

The nanowires were deformed under tensile loading at a constant strain-rate until complete failure was observed. This was achieved by applying periodic boundary conditions along the axis of the nanowire, relaxing the nanowire for 10000 MD steps, then applying a strain of 0.5% to the simulation box along the periodic direction, which in turn stretched the nanowire by the same level of strain; using a time step of $1fs$, this results in an average strain-rate of $0.05\%ps^{-1}$. This procedure of relaxation and stretching was applied sequentially until complete failure of each nanowire. A trial simulation was also performed at $0.005\%ps^{-1}$, but the difference between the two strain-rates was found to be negligible (less than 2% difference in strain at failure), especially when considering the drastic increase in the computation time required for the low strain-rate simulation. All simulations were performed using an NVE ensemble with atomic velocity rescaling every 10 MD steps in order to maintain the system temperature at 300K.

A Tersoff-type inter-atomic potential [Tersoff (1989)] was used to model the atomic interactions for all three material systems. The Tersoff parameters used for GaAs and InAs were based on the work of Nishidate and Nikishkov (2007), while the parameters used for SiC were based on the work of Tersoff (1989). The inter-atomic potentials were validated for all three material systems by calculating the elastic modulus and Poisson's ratio of a bulk sample; in all three cases, the calculated values were within

1% of the experimental values.

2.3 Results and Discussion

2.3.1 Wurtzite Nanowires

A typical failure sequence of an InAs WZ nanowire is shown in Figure 2.1 - the failure sequence is very similar for all three material systems. All three material systems fail in a brittle fashion through crack nucleation and propagation. In order to clarify the nucleation and propagation of cracks, Figure 2.1 presents a side view of a cross-sectional cut of the nanowire during deformation. We can observe the nucleation of three distinct cracks in Figure 2.1(a); two smaller cracks on the left, and one larger crack on the right. As deformation proceeds, the larger crack on the right propagates across the sample, as shown in Figure 2.1(b), until complete failure of the nanowire, as observed in Figure 2.1(c). The cracks observed in all three material systems lie on (111) planes perpendicular to the loading direction, and are thus Mode-I cleavage cracks.

All cracks nucleate on the surfaces of the nanowires, as expected, but it is interesting to note that *the cracks on the WZ nanowires all nucleate at the edges where two* $\{11\overline{2}\}$ *surface facets intersect, never on the facets themselves*; this is clearly shown in Figure 2.2 for all three material systems. In order to understand why cracks nucleate in this manner, we will calculate and compare the energy required to nucleate cracks at different locations on WZ nanowires. Let us suppose that cracks of arbitrary length a nucleate at an edge and at a facet, as shown schematically in Figure 2.3(a); the corresponding areas covered by the cracks are denoted by $A1$ and $A2$, respectively. The energy cost of nucleating a crack of area $A1$ at an edge is:

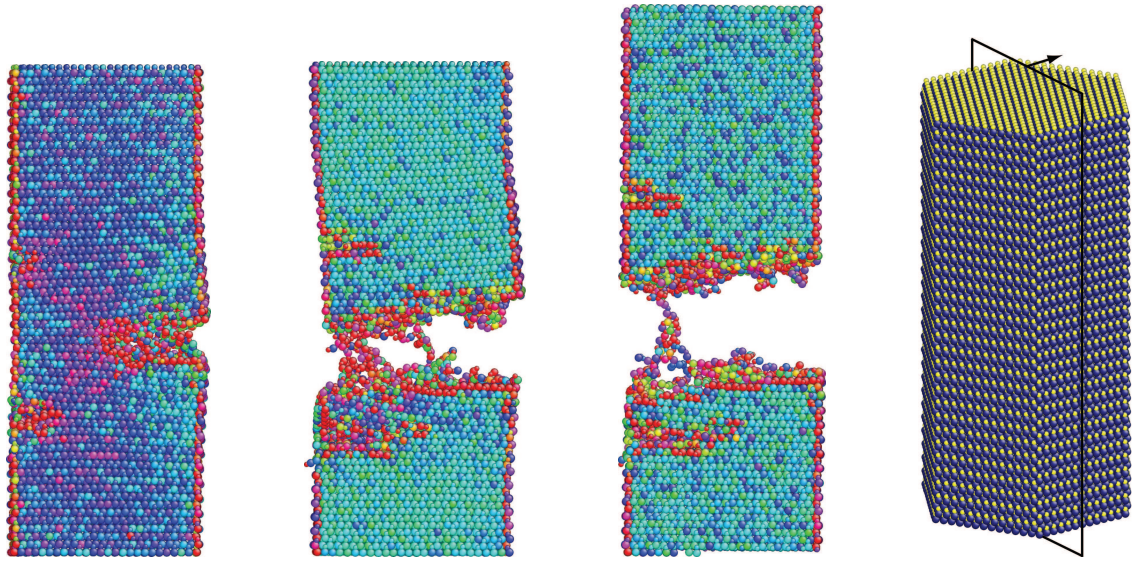

(a) Crack nucleation (b) Crack propagation (c) Complete failure (d) Location of cutting plane

Figure 2.1: Failure sequence of an InAs WZ nanowire. The atoms in (a)-(c) are colored by atomic energy; high energy surface atoms are red, while lower energy bulk atoms are blue. This nanowire has a radius of 50Å (refer to Figure 2.3(a) for the definition of nanowire radius), and is 210Å long.

$$\Omega_{A1} = 2\gamma\sqrt{3}a^2 \tag{2.1}$$

Here, γ is the surface energy. The energy cost of nucleating a crack of area $A2$ at a surface facet is:

$$\Omega_{A2} = \frac{2\gamma(2R+a)a}{\sqrt{3}} \tag{2.2}$$

The ratio of the crack nucleation energy at each site is:

$$\frac{\Omega_{A1}}{\Omega_{A2}} = \frac{3}{2(\frac{R}{a})+1} \tag{2.3}$$

It is evident that for $R \gg a$, the ratio Ω_{A1}/Ω_{A2}, is small. In our case, the radius of the nanowire is 50Å, and if we assume an incipient crack length of roughly 5Å

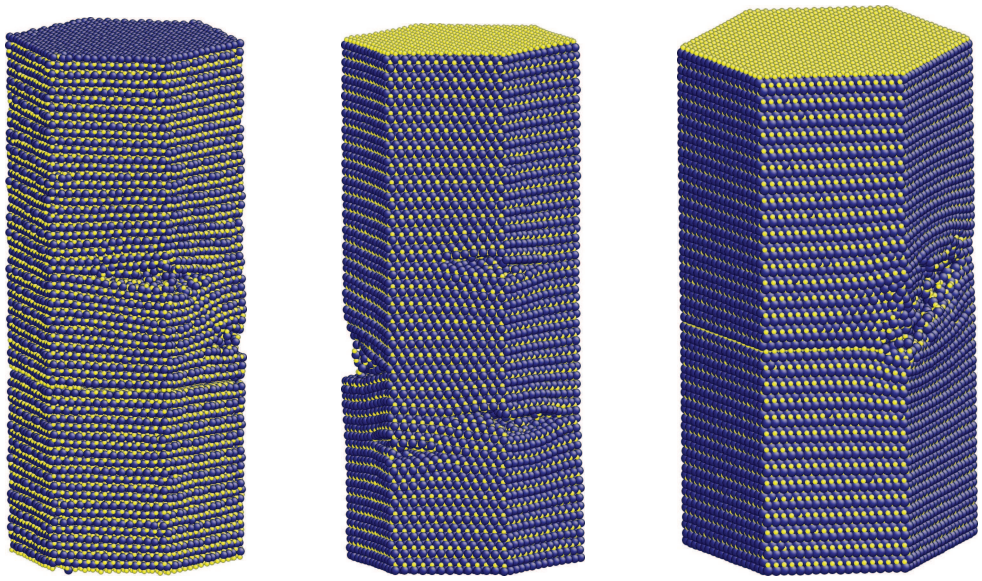

(a) GaAs (b) InAs (c) SiC

Figure 2.2: Crack nucleation on WZ nanowires. All cracks nucleate at the edges where two surface facets intersect. Each nanowire is comprised of 60 atomic bi-layers along its axis, and has a radius of 50Å (refer to Figure 2.3(a) for the definition of nanowire radius).

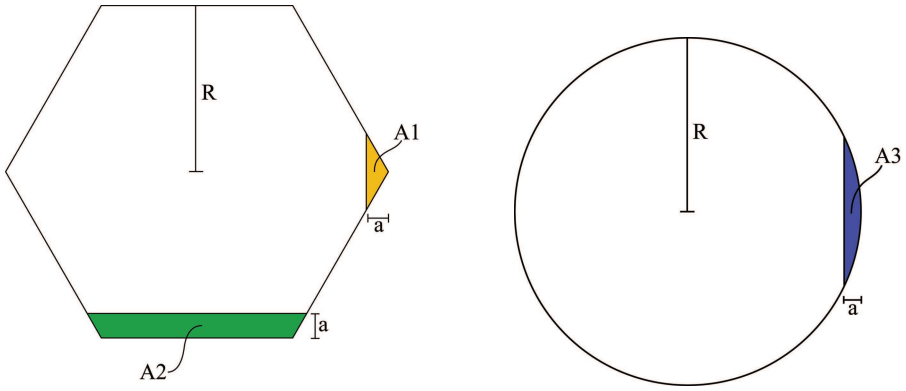

(a) WZ nanowire (b) Circular nanowire

Figure 2.3: Crack nucleation on WZ and circular nanowires. All symbols are explained within the text.

(this is on order of the atomic spacing in these materials), then the ratio Ω_{A1}/Ω_{A2} is 0.14. This result indicates that the energy required to nucleate a crack at an edge of a WZ nanowire is nearly a tenth of the energy required to nucleate the same length of

crack on a surface facet. The corollary to this explanation is that for a given amount of energy, a much larger crack can be nucleated at an edge as opposed to a facet. Based on this analysis, we can conclude that it is energetically much more favorable to nucleate a crack on an edge as opposed to a surface facet.

It is useful to consider the effect of surface morphology on crack nucleation in a more general sense. To this end, we use the same argument as before for a circular nanowire, and referring to the schematic in Figure 2.3(b), we find that the energy cost of nucleating a crack of arbitrary length a, covering an area $A3$ is:

$$\Omega_{A3} = 2\gamma\Big[\frac{\pi R^2}{2} - (R-a)\sqrt{(2R-a)a} - R^2\sin^{-1}(\frac{R-a}{R})\Big] \tag{2.4}$$

Using the same values for R and a as before, the ratio Ω_{A1}/Ω_{A3} is 0.30, which indicates that the $\{11\overline{2}\}$ surface facets of WZ nanowires significantly lower the energy required to nucleate cracks when compared to non-faceted nanowires.

While we have focused our attention thus far on the specific surface facets of WZ nanowires, we now generalize our results to arbitrary shapes and facet orientations. Let us consider the nucleation of a crack of arbitrary length a at the intersection of two surface facets separated by an interior angle θ. For this configuration, the energy cost of nucleating a crack at an edge is:

$$\Omega_\theta = 2\gamma a^2 \tan\left(\frac{\theta}{2}\right) \tag{2.5}$$

For the case of a WZ nanowire, the angle θ is 120°, which reduces Eq. 2.5 to the previous result of Eq. 2.1. Clearly, as the interior angle formed by the intersection of surface facets becomes more acute, the energy required to nucleate a crack diminishes. For example, Verheijen et al. (2007) have observed GaP-GaAs core-shell nanowires with an equilateral triangular cross-section, for which the interior angle is 60°; if we once again assume a 5Å long incipient crack and compare the nucleation energy to

that of a circular nanowire of 50Å radius, we find that the ratio of the two crack nucleation energies, $\Omega_\theta/\Omega_{A3}$, is 0.098, which is even lower than the previous ratio of a WZ nanowire to a circular nanowire.

2.3.2 Zinc-Blende Nanowires

A typical failure sequence of an InAs ZB nanowire is shown in Figure 2.4; as was the case for the WZ nanowires, the failure sequence of the ZB nanowires is very similar for all three material systems. In contrast to WZ nanowires which have a constant cross-sectional shape, ZB nanowires have surface facets that intersect to form concave and convex edges. In Figure 2.4(a), incipient cracks can be observed at the concave edges of the nanowire at the intersection of two opposing {111} surface facets and a twin plane. One of the cracks propagates across the nanowire as shown in Figure 2.4(b). The large crack in the middle of the nanowire in Figure 2.4(b) looks as though it nucleated in the bulk and not at a surface; however, it is actually a crack that has nucleated on the surface of the nanowire (in the same position, at the intersection of surface facets and a twin plane) on the backside, and is propagating forward out of the page. Complete failure of the ZB nanowire is shown in Figure 2.4(c), and the fracture surface is virtually flat and completely perpendicular to the loading direction, indicating a near-perfect cleavage across the (111) plane.

All the cracks on the ZB nanowires nucleate at the concave edges where the surface facets and twin planes intersect, as clearly illustrated in Figure 2.5. We can observe that cracks nucleate at nearly all of the concave edges of the nanowires, but eventually only one of them propagates across the entire cross-section of the nanowire. We will use an approximate elastic stress-field solution in order to understand the underlying reasons why cracks always nucleate at the concave edges. For a sharp crack in an infinite medium, it is known that the stress at the crack-tip is square-root-singular;

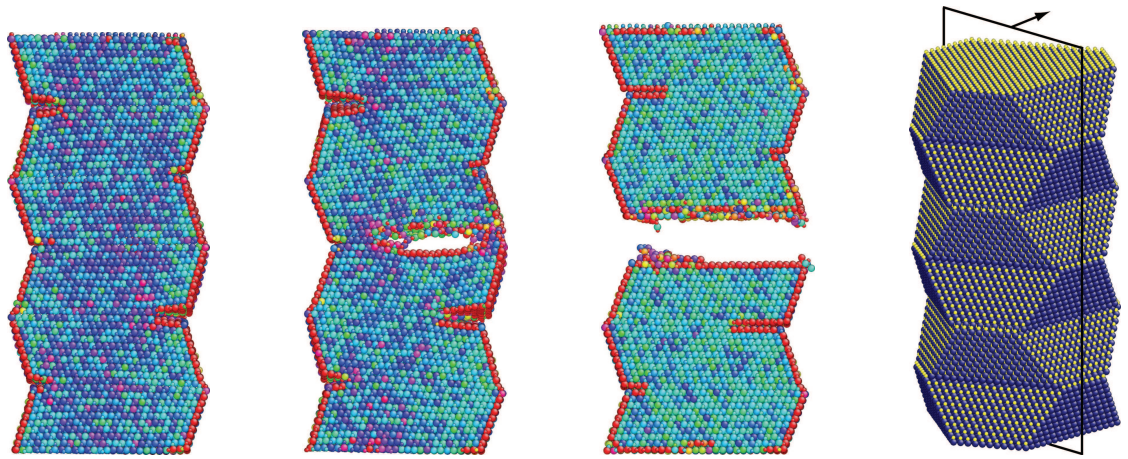

(a) Crack nucleation (b) Crack propagation (c) Complete failure (d) Location of cutting plane

Figure 2.4: Failure sequence of an InAs ZB nanowire. The atoms in (a)-(c) are colored by atomic energy; high energy surface atoms are red, while lower energy bulk atoms are blue. This nanowire has an average radius of 50Å (refer to Figure 2.3(a) for the definition of nanowire radius), and is 210Å long.

we have calculated the elastic stress-field at a notch in an infinite elastic medium in order to determine whether a stress-singularity exists at the concave edges.

If a singularity exists, its nature can be assessed by analyzing a region very close to the notch, which is equivalent to considering a symmetric notch in an infinite elastic medium, represented schematically in Figure 2.6. In our case, the angle α is 109.5°, which corresponds to the concave angle created at the intersection of two opposing $\{111\}$ facets on the surfaces of ZB nanowires. The elastic stresses within the medium have been calculated by Williams (1952) as the following:

$$\sigma_{r\theta} = r^{\lambda-1}[A\lambda(\lambda+1)\sin(\lambda+1)\theta + B\lambda(\lambda-1)\sin(\lambda-1)\theta] \tag{2.6}$$

$$\sigma_{\theta\theta} = r^{\lambda-1}[A\lambda(\lambda+1)\cos(\lambda+1)\theta + B\lambda(\lambda+1)\cos(\lambda-1)\theta] \tag{2.7}$$

In the preceding formulae, r is the distance from the notch-tip, θ is the angular

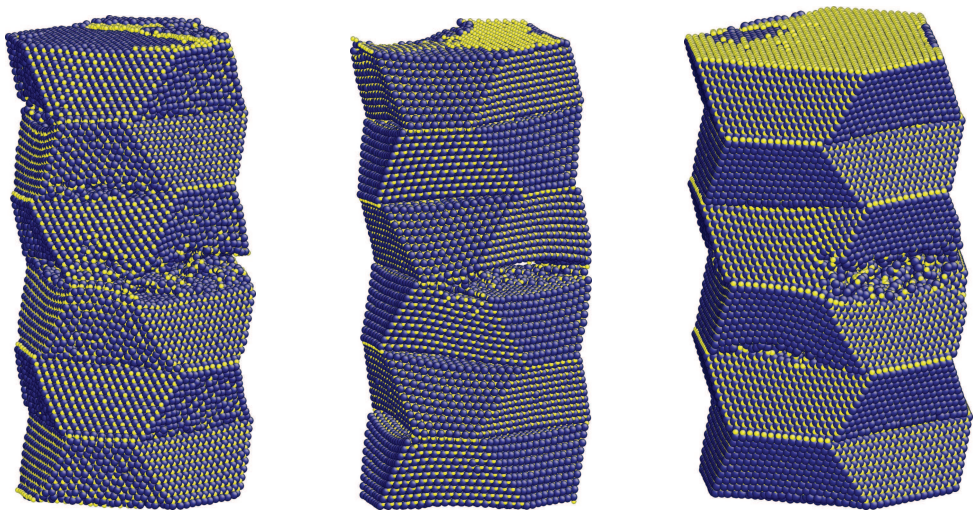

(a) GaAs (b) InAs (c) SiC

Figure 2.5: Crack nucleation on ZB nanowires. All cracks nucleate at the concave edges where two opposing surface facets intersect. Each nanowire is comprised of 60 atomic bi-layers along its axis, and has an average radius of 50Å (refer to Figure 2.3(a) for the definition of nanowire radius).

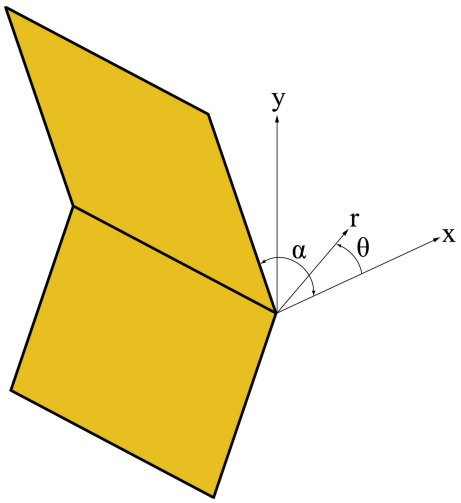

Figure 2.6: Schematic of a notch in an infinite elastic medium.

coordinate, λ represents the eigenvalues, and A and B are arbitrary constants. The traction-free boundary conditions at the surface of the notch are: $\sigma_{r\theta} = \sigma_{\theta\theta} = 0$ at $\theta = \alpha$. Applying these boundary conditions to the stresses given in Eq. 2.6 and Eq. 2.7 results in a matrix equation for the two unknown constants, A and B. By equating

the determinant of this matrix to zero in order to avoid a trivial solution, we arrive at the following characteristic equation:

$$\lambda \sin(2\alpha) + \sin(2\lambda\alpha) = 0 \tag{2.8}$$

Solving this equation numerically for the eigenvalues, λ, reveals that the stress-state at the notch-tip is proportional to $r^{-0.30}$, thereby confirming that the stresses at the concave edges of ZB nanowires are singular. We have also calculated the stress-state at the convex edges of the ZB nanowires by setting the value of α to 70.5° in Eq. 2.8. In this case, the smallest eigenvalue, λ, was found to be 1, which corresponds to a finite stress state (i.e., no singularity). These results prove that cracks will always nucleate at the singular concave edges, never at the convex edges, which is exactly what we observe in our MD simulations.

The stress-strain curves for the WZ and ZB nanowires are shown in Figure 2.7 for all three material systems. The strongest and most ductile of the three materials is SiC, while the weakest and least ductile is InAs. In the case of the ZB nanowires, we have also examined the effects of twin-plane spacing on the failure strength of the nanowires and found only a minor effect; for example, reducing the total number of twins in a GaAs ZB nanowire from 6 to 4 reduced the failure stress by only 0.5GPa. The general trend among the three materials is that the WZ nanowires can withstand higher levels of stress and greater levels of strain at failure. This result is a consequence of the singular stress-states present in ZB nanowires. The facets in the WZ nanowires facilitate crack nucleation by lowering the energy required to create free surfaces, but the stress-states within the WZ nanowires are still finite, therefore it is easier to nucleate a crack on a ZB nanowire due to the stress singularities that are inherent to its geometry.

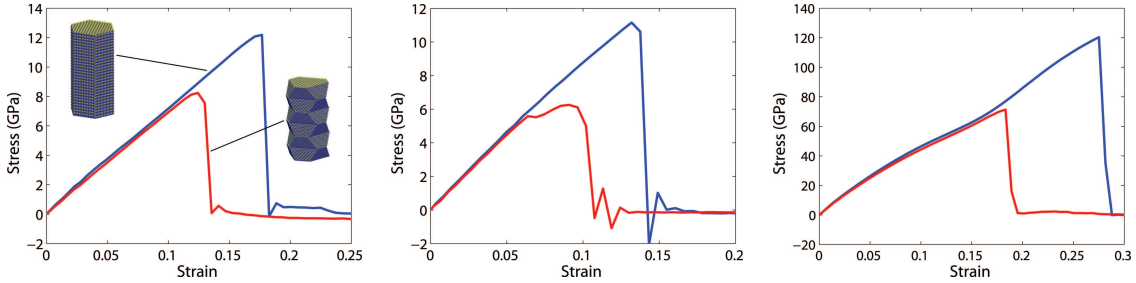

(a) GaAs (b) InAs (c) SiC

Figure 2.7: Stress-strain curves of III-V nanowires. The blue curves correspond to WZ nanowires, while the red curves correspond to ZB nanowires. For each material, the lengths of the WZ and ZB nanowires are identical, and the radius of the WZ nanowire is the same as the average radius of the ZB nanowire.

2.4 Summary

We have used MD simulations to study how the innate surface facets of III-V WZ and ZB nanowires influence their mechanical strength and failure. In WZ wires, the intersections between two adjacent $\{11\bar{2}\}$ surface facets lead to an energetically favorable site for crack nucleation. It has been shown that for constant polygonal cross-sections, surface facets always aid crack nucleation. In ZB wires, the intersections between two opposing $\{111\}$ surface facets create a stress singularity that favors crack nucleation during deformation. This singularity makes the ZB nanowires weaker and less ductile than WZ nanowires. These results hold for three different III-V material systems and are expected to be general for all such materials.

Chapter 3

Failure of Graphene Sheets Containing Grain Boundaries

3.1 Introduction

Graphene continues to be one of the most widely researched areas in materials science today. It is the thinnest material ever synthesized, yet the one of the strongest ever measured [Geim (2009), Lee et al. (2008)], and it exhibits exceptional electronic, thermal, and optical properties [Geim (2009), Geim and Novoselov (2007)]. However, despite the prolific research efforts, growing large-area, single-layer graphene sheets remains a challenge. Recently, a chemical vapor deposition (CVD) technique has been devised that exploits the low solubility of carbon in metals such as nickel [Yu et al. (2008), Kim et al. (2009)] and copper [Li et al. (2009), Levendorf et al. (2009)] in order to grow graphene on metal foils. A consequence of this technique is that the large-area graphene sheets contain grain boundaries, since each grain in the metallic foil serves as a nucleation site for individual grains of graphene [Li et al. (2009)].

Tilt grain boundaries in graphite had been observed in scanning tunneling microscopy (STM) experiments over 20 years ago by Albrecht et al. (1988), and since then several groups have performed similar microscopy studies [Osing and Shvets (1998), Simonis et al. (2002), Pong et al. (2007), Cervenka and Flipse (2009), Wong et al. (2009)]. More recently, Hashimoto et al. (2004) have observed individual dislocations in graphene using transmission electron microscopy (TEM), and the structure, as well as the electronic, magnetic, and dynamical properties of grain boundaries in graphene have been investigated by a number of other research teams [Yazyev and Louie (2010), Malola et al. (2010), Cervenka et al. (2009)]. With all this previous work established, a natural question to ask is: how do these grain boundaries influence the mechanical properties of graphene? Given the fact that graphene is one of the stiffest (modulus $\sim 1TPa$) and strongest materials (strength $\sim 100GPa$), in order to use CVD-synthesized graphene sheets in NEMS, sensors, and as pressure barriers, it is important to know how the grain boundaries influence these fundamental mechanical properties.

Although a number of studies have been carried out on the mechanics of dislocations and defects in carbon nanotubes [Li et al. (2005), Huang et al. (2008), Zhang, Mielke, Khare, Troya, Ruoff, Schatz and Belytschko (2005)] and graphene [Zhang et al. (2006)], the mechanical properties of hydrogen-functionalized graphene [Pei et al. (2010)], as well as the fracture and failure of graphene and carbon nanotubes with multiple vacancies [Xiao et al. (2009)] and Stone-Wales defects [Xiao et al. (2009, 2010), Lu and Bhattacharya (2005)], the effect of grain boundaries on the mechanical properties of graphene has been largely neglected. In this chapter, we address this outstanding problem using molecular dynamics and first-principles calculations. Contrary to the intuitive picture based on continuum models that more defective structures lead to greater deterioration of mechanical properties, we find that as the

grain boundary angles, and hence the number of defects per unit-length, increase, the strengths of the graphene sheets also increase. We have identified the underlying reason for this counterintuitive phenomenon by analyzing the initial strains within the carbon-carbon bonds along the grain boundaries. Our first-principles calculations show that higher-angle tilt grain boundaries are able to better accommodate the strained 7-member rings, which explains the increased strength. Our results indicate that CVD-grown 'polycrystalline' sheets can be comparable in strength to pristine graphene provided that they are comprised largely of higher-angle tilt grain boundaries.

3.2 Computational Methods

Molecular dynamics (MD) simulations were performed using the MD package, LAMMPS [Plimpton (1995)]. All simulations were performed on 80Å square graphene sheets; the tilt grain boundaries were placed in the middle of the sheets and were oriented parallel to the Y-direction. The graphene sheets were deformed under tensile loading in directions perpendicular (along the X-axis) and parallel (along the Y-axis) to the grain boundaries at a constant strain-rate until complete failure was observed. A 2.5Å wide strip of material at each end of the sheet was constrained against motion along the direction of deformation (but free to move in the direction perpendicular to the direction of deformation) by enforcing zero force and velocity on the atoms in these regions. With these constraints in place, the sheets were subsequently relaxed for 10000 MD steps, then a homogeneous strain of 0.5% was applied to the graphene sheets by scaling all atomic coordinates accordingly; using a time step of $1fs$, this results in an average strain-rate of $0.05\%ps^{-1}$. This procedure of relaxation and stretching was applied sequentially until complete failure of each graphene sheet. All MD simulations were performed using an NVE ensemble.

An adaptive intermolecular reactive bond order (AIREBO) potential [Stuart et al. (2000)] as implemented in LAMMPS, was used to model the atomic interactions in graphene. Following the work of Pei et al. (2010), we have used an interaction cut-off parameter of 1.92Å. In order to calculate the stress-strain curves during deformation, the stress on each individual carbon atom was first calculated according to the following Virial stress expression [Basinski et al. (1971), Chandra et al. (2004)]:

$$\sigma_{ij}^{\alpha} = \frac{1}{\Omega^{\alpha}}\left(\frac{1}{2}m^{\alpha}v_i^{\alpha}v_j^{\alpha} + \sum_{\beta=1,n} r_{\alpha\beta}^{j} f_{\alpha\beta}^{i}\right) \tag{3.1}$$

In the equation above, i and j denote the indices in the Cartesian coordinate system, while α and β are the atomic indices; m^{α} and v^{α} are the mass and velocity of atom α, respectively; $r_{\alpha\beta}$ and $f_{\alpha\beta}$ are the distance and force between atoms α and β, respectively; and Ω^{α} is the atomic volume of atom α. Once the stress on each atom was computed, we then averaged the stress over the entire sheet every 500 MD time-steps, and averaged these values over the latter half of the relaxation period of 10000 time-steps in order to obtain both a spatial and temporal average of the stresses. This method provides a single stress value for every strain increment, thereby allowing us to construct a stress-strain curve for the graphene sheets.

The inter-atomic potential and simulation method as a whole were validated by deforming pristine graphene and comparing the results to experiments. Our methods predicted an elastic modulus of $0.8TPa$, an ultimate strength of $125GPa$, and a strain-at-failure of 25% for zig-zag oriented graphene. Our predicted value of elastic modulus is within 20% of the experimental value reported by Lee et al. (2008), while the ultimate strength and strain at failure match the experimental values almost exactly.

The first-principles Density Functional Theory (DFT) calculations were performed with a plane-wave basis-set using the *ab initio* simulation package, VASP [Kresse

and Furthmuller (1996)]. Projector-Augmented Wave potentials (PAW) [Kresse and Joubert (1999)] were used to represent the ionic cores, and Perdew-Burke-Ernzerhof (PBE) exchange-correlation functionals [Perdew et al. (1996)] were used for gradient approximations. For all the DFT calculations, a vacuum of 12Å was used in the direction perpendicular to the graphene sheets, and the sheets were periodic in the direction parallel to the grain boundaries (the Y-direction). In the X-direction, we saturated the non-periodic graphene edges with hydrogen atoms in order to ensure that all carbon atoms were sp^2 bonded (the Z-direction is normal to the graphene basal-plane). A kinetic energy cutoff of 500eV was used in all DFT calculations. The structures were relaxed using the conjugate-gradient algorithm until the atomic forces were smaller than 0.04eV/Å. A convergence study was performed in which the k-point mesh was varied from $1 \times 5 \times 1$ up to $1 \times 20 \times 1$, with the key results varying by no more than 0.2% (only 1 k-point has been used in the Y- and Z-directions since they are both non-periodic). A separate study was also carried out in which the width of the model (in the X-direction) was varied from 18.7Å to 28.9Å; in this case, the maximum discrepancy in the results was less than 1%.

3.3 Tilt Grain Boundary Structures in Graphene

The structures of tilt-grain boundaries in zig-zag oriented graphene are shown in Figure 3.1 for grain boundary angles of 5.5°, 13.2°, and 21.7° (the angles represent the total mismatch angles between the left and right grains). The grain boundaries consist of repeating 5-7 ring pairs that are separated by several hex-rings. As the grain boundary angle increases, the number of hex-rings separating the 5-7 defects decreases, with the ultimate limit occurring at 21.7° when only a single hex-ring separates the periodic 5-7 defects. Therefore, more severe grain boundary angles are comprised of higher defect densities. The repeating defect pairs can also be thought

of as an array of edge dislocations with horizontal Burgers vectors where the 5-rings represent the extra plane of atoms, as shown in Figure 3.1.

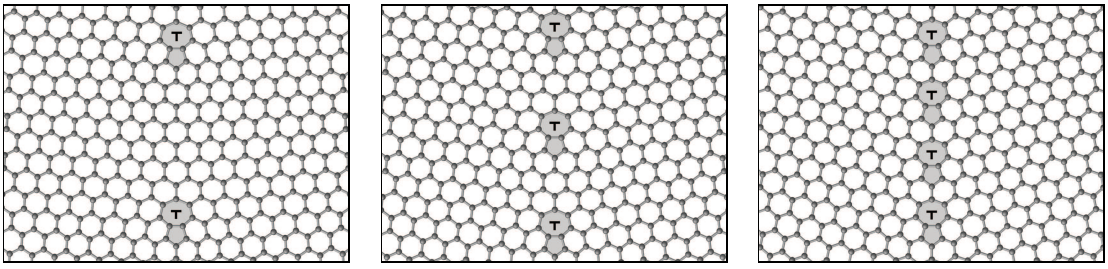

(a) 5.5° (b) 13.2° (c) 21.7°

Figure 3.1: The structures of grain boundaries in zig-zag oriented graphene sheets with varying mismatch angles.

Tilt boundaries in arm-chair oriented graphene are shown in Figure 3.2 for grain boundary angles of 15.8°, 21.4°, and 28.7°. For this orientation, the repeating defect consists of two diagonally opposed 5-7 pairs that are separated by several hex rings. As was the case for the zig-zag orientation, larger grain boundary angles consist of higher defect densities; however, for the arm-chair oriented graphene, the most severely misoriented boundary (28.7°) consists of repeating 5-7 pairs without any intermediate hex-rings. Viewing the grain boundary in terms of dislocations, the two diagonally opposed, repeating 5-7 pairs represent two partial edge dislocations, as shown in Figure 3.2. The vertical components of the Burgers vectors of the two partial dislocations nullify one-another, leaving the grain boundary vertically oriented (for a vertical boundary, the net Burgers vector must be purely horizontal).

3.4 Results and Discussion

The stress-strain curves for zig-zag oriented graphene sheets with tilt grain boundaries are shown in Figure 3.3, while those of the arm-chair oriented graphene sheets are shown in Figure 3.4. For both orientations, the simulated stress-strain curves have

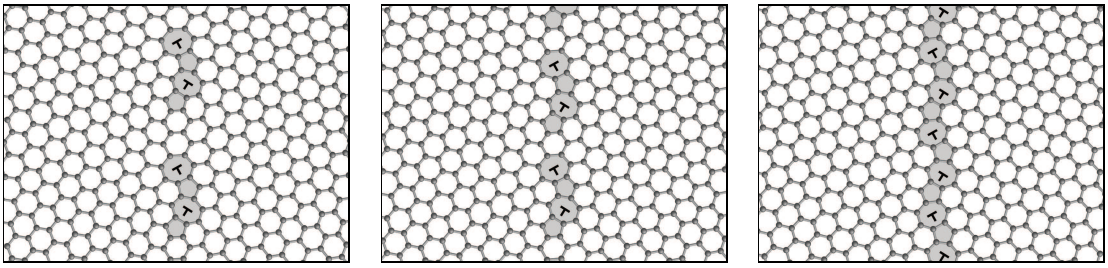

(a) 15.8° (b) 21.4° (c) 28.7°

Figure 3.2: The structures of grain boundaries in arm-chair oriented graphene sheets with varying mismatch angles.

been plotted for deformation perpendicular and parallel to the grain boundaries. In general, grain boundaries may be oriented at an angle relative to the tensile axes; to study the effect of this variation, we consider the extreme cases i.e., the grain boundaries oriented along and perpendicular to the loading axes. In both cases, the variation of the failure strength with angle is larger when the sheets are pulled perpendicular to the boundaries than when they are pulled parallel to the boundaries.

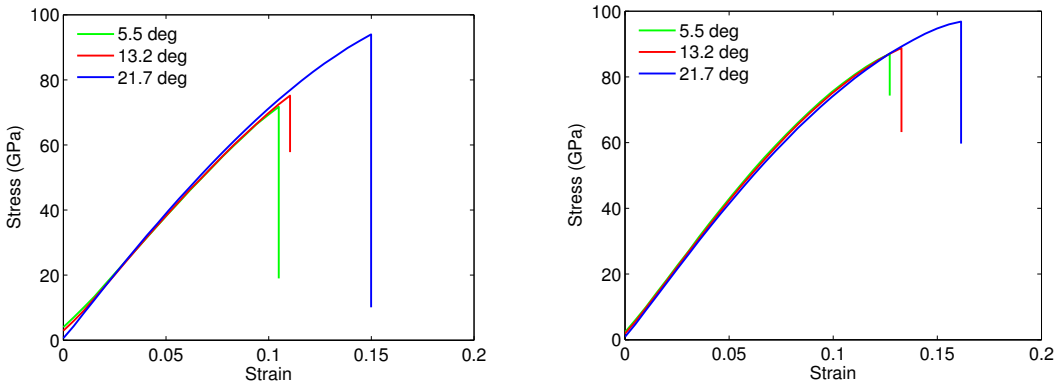

(a) Perpendicular (b) Parallel

Figure 3.3: The stress-strain curves of zig-zag oriented graphene sheets pulled perpendicular (a) and parallel (b) to the grain boundaries.

Upon initial inspection, the data in these plots looks mislabled, or it seems as though the legends have been misread, since all four plots illustrate the same completely counterintuitive result: *As the grain boundary angle, and hence the defect*

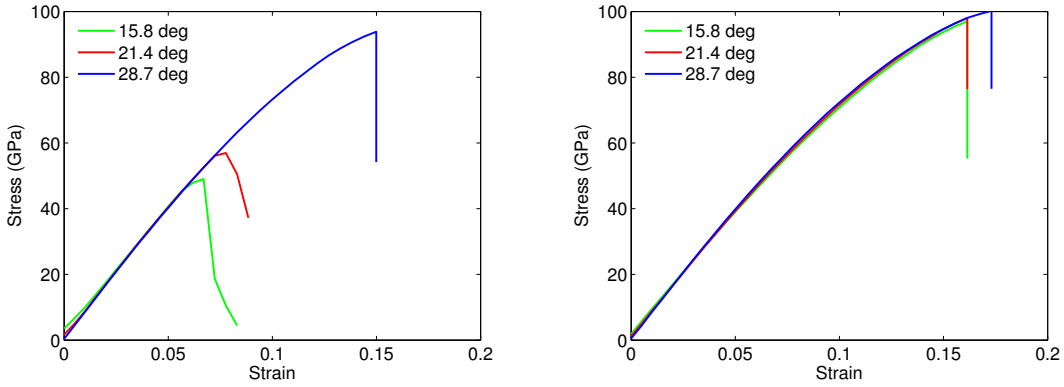

(a) Perpendicular (b) Parallel

Figure 3.4: The stress-strain curves of arm-chair oriented graphene sheets pulled perpendicular (a) and parallel (b) to the grain boundaries.

density, increases, the ultimate failure strength and strain at failure increase! One would automatically assume that as the number of defects increases, the strength of any material should *decrease*; how is it that a higher density of 5-7 defects along the grain boundaries actually *increases* the strength of graphene sheets?

To answer this question and to make an analogy to what continuum models predict about the scaling of strength with defect density, we consider a fracture-mechanics-based approach in which we model the 7-member rings along the grain boundary as an infinite array of Griffith cracks. This is a reasonable continuum-level analogue of the 7-member rings, since these rings are larger than the hex-rings and so they can be represented as a crack or a void within the material. This assumption is also consistent with the fact that failure in the graphene sheets *always* begins at the 7-member rings (we will discuss this phenomenon in more detail later on in this chapter). We therefore consider an infinite array of Griffith cracks (the crack tips aligned along the boundary), each of length $2a$, and separated by a length $2h$ from one-another. The common method that is used to determine whether a crack advances upon application of a remote stress, σ_∞, is to compute the stress-intensity factor, K_I. If K_I exceeds K_{IC} - the experimentally measured fracture toughness for a given material -

then crack propagation will ensue. The stress-intensity factor for the arrangement of cracks outlined above can be computed using standard fracture mechanics techniques [Broberg (1999)], and is presented in the following equation:

$$K_I = \sigma_\infty \sqrt{(2h) tan\left(\frac{\pi a}{2h}\right)} \tag{3.2}$$

A plot of the non-dimensional stress-intensity factor, $K_I/\sigma_\infty\sqrt{a}$, versus normalized crack-spacing, h/a, is presented in Figure 3.5. As the inter-crack spacing, $2h$, decreases, the stress-intensity factor, K_I, increases due to the interaction of the stress fields of adjacent cracks. Based on the plot in Figure 3.5, graphene sheets *should* be weaker as the defect distribution becomes more dense. Clearly, this fracture mechanics analogy fails to explain our results, and so the explanation that we seek does not lie within continuum mechanics techniques, but on the atomic-level details of bond rupture and failure. We therefore focus on the sequence of atomic-scale events that leads to tensile failure.

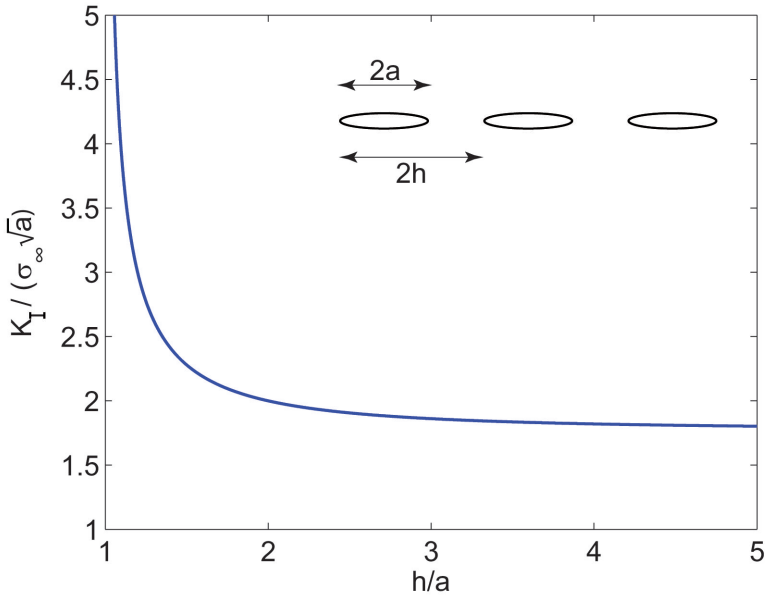

Figure 3.5: Non-dimensional stress-intensity factor versus normalized crack-spacing.

Figure 3.6 shows the first signs of failure within the zigzag oriented graphene sheets during deformation perpendicular to the boundaries. What is striking is that the first bonds to break (the top-most bonds of the 7-rings on either the left or right side, highlighted in red) are always the same ones for all three grain boundary angles. Once these bonds have been broken, complete failure of the sheets proceeds rapidly along the grain boundaries.

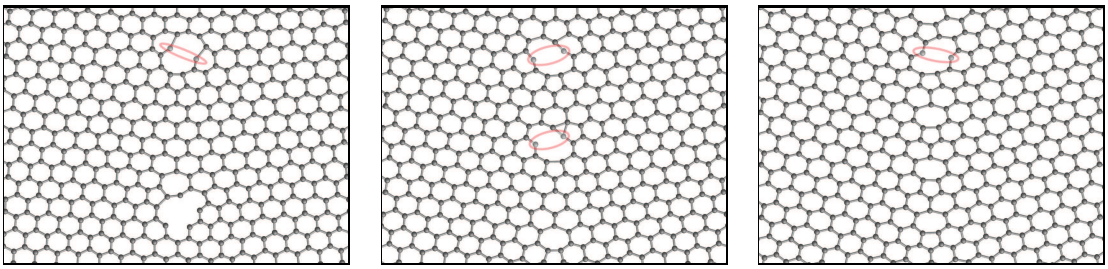

(a) 5.5° (b) 13.2° (c) 21.7°

Figure 3.6: The initial stages of failure in zig-zag oriented graphene sheets pulled perpendicular to the grain boundaries.

The first signs of failure for the zig-zag oriented graphene sheets pulled parallel to the grain boundaries are shown in Figure 3.7. As was the case previously, we observe that for each of the three grain boundary angles, the same bonds in the 7-rings (the most vertically aligned side bonds in this case, highlighted in red) are the first to break, although it should be noted that the critical bonds in this case are different from those of the sheets that were pulled perpendicular to the boundary. The location of the critical bonds is dependent on the orientation of the graphene (zig-zag or arm-chair) and the loading direction (parallel or perpendicular to the grain boundary); for each specific combination of orientation and loading direction, the critical bonds are the same for all three grain boundary angles.

We now focus our attention on the incipient failure of arm-chair oriented graphene sheets pulled perpendicular and parallel to the boundary, as shown in Figures 3.8 and 3.9, respectively. As was the case for zig-zag oriented graphene, we observe that for

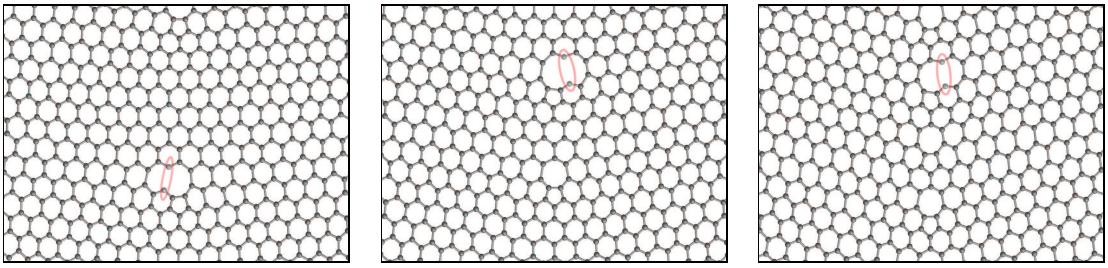

(a) 5.5° (b) 13.2° (c) 21.7°

Figure 3.7: The initial stages of failure in zig-zag oriented graphene sheets pulled parallel to the grain boundaries.

each loading direction, the same critical bonds (those highlighted in red) initiate failure in the arm-chair oriented graphene sheets regardless of the grain boundary angle. There is, however, an exception in the case of the largest grain boundary angle for both loading directions, which actually fail away from the boundaries, within the highlighted regions in Figures 3.8(c) and 3.9(c).

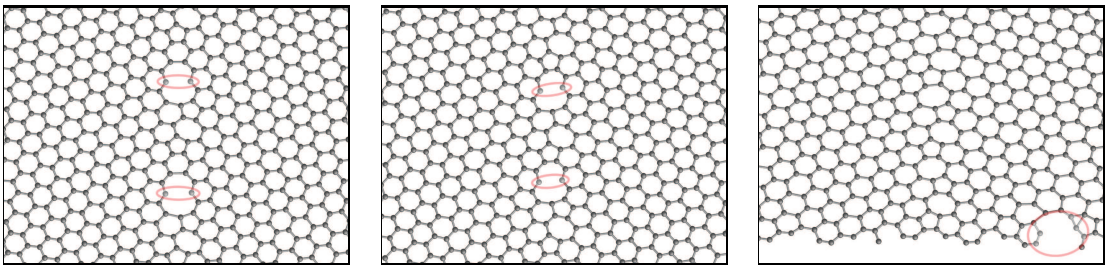

(a) 15.8° (b) 21.4° (c) 28.7°

Figure 3.8: The initial stages of failure in arm-chair oriented graphene sheets pulled perpendicular to the grain boundaries.

Having identified the critical bonds, we now focus on the initial strains in these bonds as a function of the grain boundary angle, and uncover clues towards understanding the anomalous strength of tilt grain boundaries in graphene. As the grain boundary angle increases, the initial lengths of the critical bonds decrease towards the sp^2 carbon-carbon bond-length in pristine graphene. Prior to any applied deformation, for loading perpendicular to the boundary, the strain in the critical bonds of the

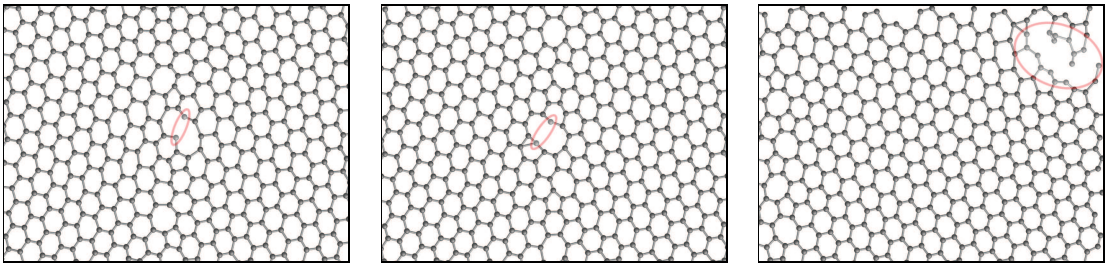

(a) 15.8° (b) 21.4° (c) 28.7°

Figure 3.9: The initial stages of failure in arm-chair oriented graphene sheets pulled parallel to the grain boundaries.

zigzag oriented graphene sheets with grain boundary angles of 5.5°, 13.2°, and 21.7°, are 12.2%, 10.3%, and 5.4%, respectively. Our DFT simulations validate these results and the general trend, with calculated strains of 9.5%, 8.7%, and 5.4% as the grain boundary angle increases. Naturally, as the pre-strain in the material decreases, the strain at failure and ultimate strength will increase. It is the level of preexisting strain within the critical bonds of the 7-member rings that accounts for the counterintuitive results we have observed in our simulations.

The initial strains in the critical bonds for zig-zag graphene pulled parallel to the boundary are 2.1%, 1.7%, and 0.7% for the 5.5°, 13.2°, and 21.7° grain boundary angles, respectively. The strains calculated through DFT are slightly higher at 3.2%, 2.2%, and 1.7%, however, the trend matches that of the MD simulations perfectly. Although the level of initial strain is lower for these critical bonds than those discussed in the preceding paragraph, the general trend of decreasing strain with increasing grain boundary angle is the same, and is consistent with the stress-strain results plotted in Figure 3.3.

In the undeformed state, the critical bonds in arm-chair graphene pulled perpendicular to the boundary are strained by a factor of 23.4%, 9.3%, and 1.7% for the 15.8°, 21.4°, and 28.7° boundary angles, respectively. Once again, we observe

the trend of decreasing initial strain with increasing grain boundary angle. Interestingly, the graphene sheet with a 28.7° grain boundary angle begins to fail away from the boundary, at the location highlighted in Figure 3.8(c). This is due to the fact that in this case, the bond lengths in the 7-member rings are very close to those of pure graphene (the previously mentioned strain of 1.7% being the largest among the 7 bonds), and two of the bonds are actually initially shorter than those of pure graphene. Reexamination of the stress-strain curve corresponding to this grain boundary angle and pulling direction (shown in Figure 3.4(a)) indicates a strain at failure of 15.5%, and an ultimate strength of $95GPa$, values that are approaching the strength of pure arm-chair graphene. Based on these results, we can conclude that grain boundaries with a mismatch angle of 28.7° do not affect the strength of arm-chair oriented graphene sheets appreciably, whereas those with lower separation angles weaken them significantly.

For arm-chair graphene pulled parallel to the boundary, the critical bonds in the 15.8° and 21.4° are strained by factors of 5.4% and 4.0%, respectively; the 28.7° sheets begin to fail away from the boundary (within the highlighted region in Figure 3.9(c)), due to the fact that for the most severe grain boundary angle, this bond is actually the same length as those in pure graphene. Thus, we have shown that the general trend of decreasing initial strain with increasing grain boundary angle is perfectly consistent for zigzag and arm-chair oriented graphene sheets, and that the initial bond lengths fully explain the counterintuitive results observed in our MD simulations.

3.5 Summary

In summary, we used MD and DFT calculations to study the mechanical strength of grain boundaries in zig-zag and arm-chair oriented graphene sheets. For both orientations, we have found that the strain at failure and ultimate strength of graphene

increases with grain boundary angle. We have looked in detail at the atomic-scale bond-breaking processes that lead to failure and have identified the critical bonds that determine the ultimate strength of the grain boundaries. Based on these analyses, it is clear that the initial strain in these bonds determines the failure strength - the higher the strain, the lower the strength. Higher grain boundary angles can better accommodate the 7-ring defects that comprise the grain boundaries, therefore the initial strain in the critical bonds decreases with increasing angle. Fracture mechanics methods were unable to predict the trends from our simulations because the influence of strained atomic bonds is inherently absent from continuum techniques.

Chapter 4

Crack Propagation in Cylindrical Graphite Electrodes

4.1 Introduction

Lithium-ion batteries have gained prominence in electronic devices such as cell phones and laptop computers due to their high energy-density that reduces their weight by half and their volume by $20 - 50\%$ compared to other battery chemistries such as nickel-cadmium, and nickel-metal-hydride [Aifantis et al. (2007)]; they also present an attractive solution as renewable energy sources for the transportation industry [Woodford et al. (2010)]. Initially, the anodes and cathodes in such batteries were comprised entirely of lithium, however, due to safety considerations, graphite and $LiCoO_2$ have become the main materials of choice for the anodes and cathodes, respectively [Aifantis et al. (2007), Aurbach et al. (2002)]. The use of these materials in electrode particles presents a challenge to the long-term reliability of lithium-ion batteries due to diffusion-induced stress that occurs during cyclic charging [Cheng and Verbrugge (2010*a*,*b*, 2009)]. As lithium diffuses into a graphite electrode, the

material undergoes a volumetric expansion resulting in stress, which can potentially cause crack growth [Aifantis et al. (2007), Cheng and Verbrugge (2010*a*)]. Cracking has been observed in degraded electrodes [Woodford et al. (2010), Harris et al. (2010)] and is suspected as a primary source of impedance growth and capacity loss [Woodford et al. (2010)] since the formation of free surfaces within electrodes leads to the growth of a solid electrolyte interphase (SEI) [Aurbach et al. (2002), Zhang, Li, Liu, Tan and Cheng (2005), Liu et al. (2010)]. The SEI is a passivating surface film [Zhang, Li, Liu, Tan and Cheng (2005)], therefore limiting its growth is of vital importance to maintaining the capacity of lithium-ion batteries over their life-span of several years.

Several research groups have calculated the diffusion-induced stress-states within particles in order to study the mechanical degradation of electrodes. Zhang et al. (2007) and Zhang, Sastry and Shyy (2008) have used finite difference and finite element calculations to determine the intercalation-induced stress-states in spherical and ellipsoidal particles; Cheng and Verbrugge (2009) have compared the difference in the evolution of stress within spherical particles due to potentiostatic and galvanostatic charging conditions; Christensen and Newman (2006) have assessed the likelihood of fracture by using a maximum tensile stress criterion. In another study, Cheng and Verbrugge (2010*a*) have studied the propagation of cracks by calculating the strain energy density during charging and comparing the total strain energy within the particle to the energy required to propagate a crack. A similar approach has been adopted by Woodford et al. (2010), wherein the diffusion-induced stress is computed in the absence of a crack, and is then used to determine the stress intensity factor in order to study crack growth. These latter studies concerned with particle fracture are all approximate in that they ignore the effect of the crack on the calculation of the elastic stress-state.

A more complete analysis is presented by Zhao et al. (2010), who have numerically

calculated the elastic stress-state within a square particle containing a crack. The computed elastic stress is then used to calculate the energy release rate, which is a standard fracture mechanics approach for determining whether a crack will advance. Another common fracture mechanics technique has been adopted by Bhandakkar and Gao (2010), who have used an analytical cohesive zone model to study crack nucleation in a strip electrode. Both of these methods can predict whether a crack will grow or not, however, neither method can capture the progressive propagation of cracks during cyclic loading. Furthermore, none of the aforementioned studies take crack microstructure (i.e., position and orientation within the particle) into account in their failure criterions. The aim of this chapter is to present a finite element framework that allows modeling of the progressive propagation of cracks during cyclic loading, which can then be used to develop a failure criterion based on the location and orientation of cracks within electrodes.

Motivated by scanning electron microscope images of cracks in graphite anodes and $LiCoO_2$ cathodes, we have analyzed crack propagation in cylindrical graphite particles comparable in size to those presented by Harris et al. (2010). In this chapter, we present the results of coupled diffusion-stress finite-element calculations that use cohesive zone elements to model progressive crack growth during cyclic charging of graphite particles. Cohesive elements can be loaded and unloaded in such a manner as to allow for continuous damage accumulation as the crack grows during cyclic loading. We have considered the growth of small initial defects situated at various positions and orientations within the electrode particle, and have discovered that only defects that are far from the center and not highly mis-aligned relative to the radial direction will grow during cyclic charging. A failure map is presented which demarcates safe and unsafe regions corresponding to a range of locations and orientations.

4.2 Computational Methods

4.2.1 Diffusion Analysis

Finite element calculations were carried out using the commercial finite element program, ABAQUS [ABAQUS Manual (2010)]. In order to facilitate the diffusion-stress coupling, we solved the equivalent heat equation and performed a sequentially coupled thermal-stress analysis, since ABAQUS is conveniently setup for such a procedure. The general heat/diffusion equation has the following form:

$$\frac{\partial \phi}{\partial t} = \alpha \nabla^2 \phi \tag{4.1}$$

Here, ϕ represents concentration in the diffusion equation or temperature in the heat equation, and α represents the diffusion constant, D, or the thermal diffusivity, $k/\rho C_p$, of a material.

The particle was modeled as a two-dimensional cylinder with a prescribed sinusoidal variation of concentration at the periphery. The choice of the cylindrical geometry, as well as the size of the particle, was motivated by the shape and size of actual electrode particles, as shown in Harris et al. (2010), and reproduced with permission in Figure 4.1. For the analysis of radially aligned defects, the geometry was discretized using 50 elements along the radius (1 triangular element at the center, and 49 quadrilateral elements). For analyses involving radially misaligned defects, a simple radial mesh is not possible and so the particle was meshed in a more complex fashion using only quadrilateral elements of the same size as the other analyses.

With the geometry, material specifications, and loading defined, the full transient concentration (temperature) field was calculated at each node. An identical mesh was used for the diffusion (heat-transfer) and stress analyses in order to directly pass the concentration field at each node from the diffusion analysis to the stress analysis.

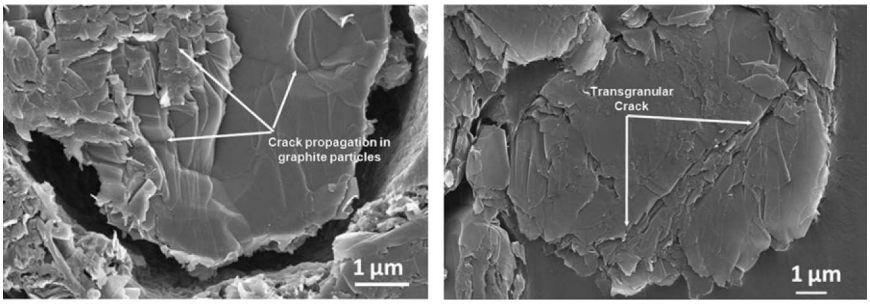

Figure 4.1: Scanning electron microscope images of cracks in cylindrical graphite particles [Harris et al. (2010)].

4.2.2 Stress Analysis

The stress analysis should be equally applicable to the anode (graphite) and cathode ($LiCoO_2$), but for the sake of concreteness, we have chosen a graphite electrode as an example in light of recent work showing the presence of internal cracks in graphitic particles, as shown in Figure 4.1 [Harris et al. (2010)]. As lithium diffuses into the graphite particle, it bonds with carbon to form LiC_6, which increases the spacing between adjacent graphene sheets from 3.35Åto 3.71Å[Kganyago and Ngoepe (2003)]. This volumetric expansion drives stress evolution within the particle, and is modeled using an equivalent thermal expansion in the following manner [Cheng and Verbrugge (2009)]:

$$\alpha \Delta T = \frac{1}{3} \Omega C \tag{4.2}$$

Here, α is the equivalent coefficient of thermal expansion, ΔT is the change in temperature, Ω is the partial molar volume of the solute, and C is the concentration of the solute. This expression equates the volumetric thermal strain (the left-hand side of the equation) and the volumetric strain as a result of LiC_6 formation. Based on the volume change associated with LiC_6 formation quoted above, Ω and α can be easily determined. By using the simulated temperature field from the heat transfer

analysis along with the coefficient of thermal expansion, the correct volumetric strain can be calculated and used to determine the stress-state within the particle.

For the majority of the analyses in this chapter, the graphite comprising the particle was modeled as a plane-stress isotropic elastic material. We have also performed one study in which fully anisotropic diffusion, expansion, and elasticity has been employed in order to observe the effects of anisotropy on our results.

Crack propagation within the particle was modeled using cohesive zone elements [ABAQUS Manual (2010)]. The idea of cohesive zones for modeling crack propagation was first introduced by Dugdale (1960) and Barenblatt (1962) in order to analyze crack growth in steel sheets containing slits, and was later adapted within a finite element framework by Needleman (1987). Cohesive zone elements are zero-thickness elements that are used to mesh regions where cracks can propagate, and they apply a traction to the adjacent material based on a traction-separation law. Figure 4.2 presents a schematic of the linear softening traction-separation law that was used in our simulations. The initial portion of the curve is linear-elastic up to the damage initiation stress, σ_i. The cohesive stiffness, K, is defined as the slope of this initial portion of the curve (note the units of K; it is defined as traction - and not force - per unit extension).

Beyond the damage initiation stress, damage accumulates within the cohesive zone elements in an irreversible manner, while their stiffness linearly decreases to zero, until the failure separation, δ_f, is reached. As adjacent cohesive elements reach the failure separation, δ_f, simulated crack propagation is observed. The area beneath the traction-separation law represents the surface energy of the material (2γ), which based on the Griffith fracture criterion, is equal to the energy release rate (G) required to propagate a crack in an elastic medium. It should be noted that due to the fact that cracks can grow under tensile or shear loading only, cohesive elements exhibit

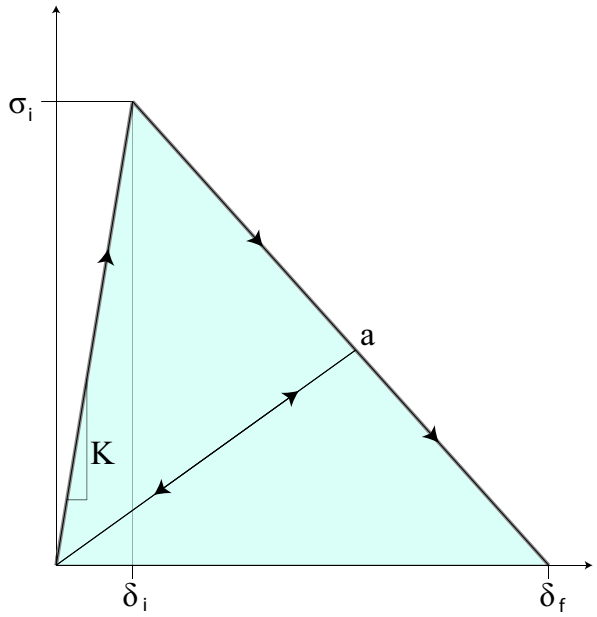

Figure 4.2: Cohesive zone traction-separation law [ABAQUS Manual (2010)].

purely linear-elastic behavior in compression, even after complete failure.

Cohesive elements can be loaded and unloaded in such a manner as to allow for continuous damage accumulation during cyclic loading. If a cohesive element is loaded beyond the damage initiation stress up to point a in Figure 4.2, and subsequently unloaded, it follows a linear-elastic path from point a to the point of zero traction and displacement. Upon reloading, the element initially follows this same path in reverse, from zero traction and displacement linearly up to point a, then along the main path of the traction-separation law; in this way, the element progressively softens and accumulates damage as it is cyclicly loaded. If an element fails on a given loading cycle and the structure is then unloaded, upon subsequent reloading the adjacent elements can fail since they have already accrued significant damage from the previous loading cycle; due to this phenomenon, we can model progressive crack propagation while a structure is cyclically loaded.

The defects within the particle were modeled by assigning a value of zero to the

damage initiation stress of certain cohesive elements. In this way, at the onset of the slightest stress within the material, these weak regions fail, thereby creating a small initial crack. These defects were placed at different locations along the radius of the particle, and at different angular orientations relative to the radial direction. A schematic of the location (the distance from the midpoint of the defect to the center of the particle), d, and orientation, θ, of a defect within the particle is shown in Figure 4.3. Our aim is to study the failure of defects as a function of these geometric parameters.

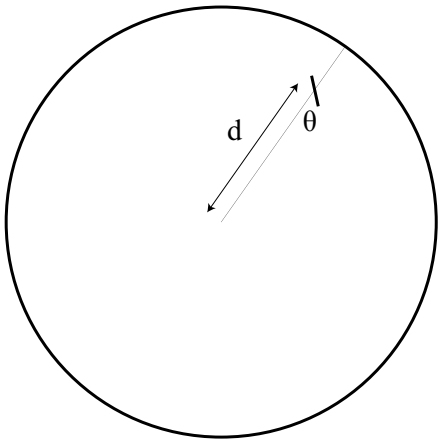

Figure 4.3: The coordinates used to define the location and orientation of a defect within the particle.

All numerical parameters used in the isotropic simulations are listed in Table 4.1. In our simulations, we have adopted potentiostatically-controlled charging [Cheng and Verbrugge (2009)], where the charging period refers to the period of the sinusoidally varying concentration at the surface of the particle, while the maximum concentration refers to the amplitude of this curve. This loading curve sinusoidally increases the lithium concentration at the surface of the particle from zero to the maximum value over a time-span of one half of the charging period, then decreases the concentration back down to zero. The charging period was chosen in order to allow sufficient time for the surface concentration value to reach the center of the particle, and the maximum

concentration corresponds to the maximum possible volumetric expansion of carbon during lithium intercalation.

Table 4.1: Isotropic model parameters

Property	Value
Particle radius	10 μm
Diffusion constant (D)	6.2×10^{-9} cm^2/s [Persson et al. (2010)]
Charging period	500 s ($14.4C$)
Number of cycles	10
Maximum concentration	0.03 mol/cm^3
Elastic modulus	33 GPa [Blakslee et al. (1970)]
Poisson's ratio	0.3 [Blakslee et al. (1970)]
Expansion coefficient (α)	1.14 cm^3/mol
Defect length	0.8 μm
Fracture energy	2.0 J/m^2
Damage initiation stress	150 MPa
Cohesive stiffness	33 $GPa/\mu m$

The expansion coefficient is the equivalent thermal expansion coefficient (α) used in the stress analysis. We have assumed a typical fracture energy to define the cohesive law, and the damage initiation stress was chosen to allow us to observe crack propagation under the specified loading. The cohesive stiffness was set in order to match the elastic modulus of the surrounding material.

The parameters used in our anisotropic calculations are listed in Table 4.2. For the anisotropic simulations, the particle was divided into five equal segments, each with a different material orientation. Figure 4.4 shows a schematic depicting the orientation of the graphite in the first segment. A local material coordinate system is defined such that the graphene sheets comprising the graphite are coplanar with the local $x'z'$ plane, and the local y' axis defines the stacking direction of the graphene. The material orientations for each of the five grains are listed in Table 4.2 as β_i (the angle between the local and global coordinate systems, as shown in Figure 4.4), where i is the segment number (segment 1 is hatched in Figure 4.4, and the numbers increase

sequentially in a counterclockwise fashion). The anisotropic diffusion constants (D_x, D_y), expansion coefficients (α_x, α_y), and elastic stiffness tensor (C_{ijkl}), are all listed in Table 4.2 with reference to the local $x'y'z'$ material coordinate system.

Table 4.2: Anisotropic model parameters

Property	Value
D_x	4.4×10^{-6} cm^2/s [Persson et al. (2010)]
D_y	8.7×10^{-12} cm^2/s [Persson et al. (2010)]
C_{1111}, C_{3333}	1060 GPa [Blakslee et al. (1970)]
C_{1122}, C_{2233}	15 GPa [Blakslee et al. (1970)]
C_{2222}	36.5 GPa [Blakslee et al. (1970)]
C_{1133}	180 GPa [Blakslee et al. (1970)]
C_{1212}, C_{1313}, C_{2323}	4 GPa [Blakslee et al. (1970)]
α_x	0
α_y	1.14 cm^3/mol
β_1	145°
β_2	217°
β_3	289°
β_4	1°
β_5	73°
Fracture energy	4.0 J/m^2
Damage initiation stress	300 MPa

Due to the higher stresses in the anisotropic analyses, the failure initiation stress of the cohesive elements was doubled, thereby doubling the fracture energy. The particle radius, loading parameters (charging period, number of cycles, maximum surface concentration), defect length, and cohesive stiffness were the same as the isotropic cases.

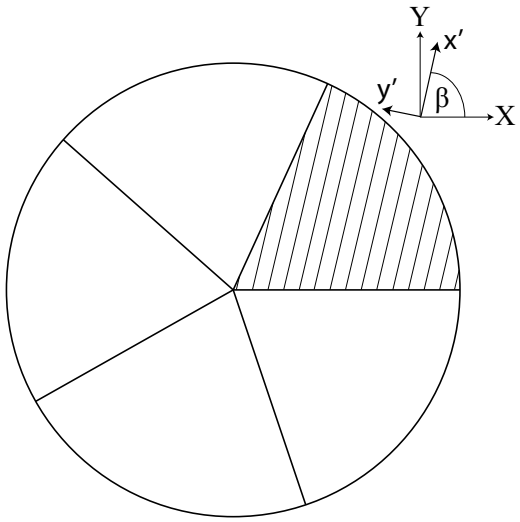

Figure 4.4: Schematic of the material orientations along with the local coordinate system used to define anisotropic material parameters.

4.3 Results and Discussion

We will begin our discussion with the propagation of radially-aligned and mis-oriented cracks, then move on to non-propagating cracks, stress during cyclic loading, and finally, we will present a failure diagram that delineates safe and unsafe crack propagation regimes, along with a discussion of the effects of the model parameters on the failure map. In addition to these results, which were all obtained using isotropic assumptions, we will also present some results obtained using fully anisotropic behavior in order to compare the qualitative differences.

4.3.1 Progressive Crack Propagation

The crack propagation sequence for a radially-aligned defect at the periphery of the particle is shown in Figures 4.5(a)-4.5(d). The initial defect can be seen under load in Figure 4.5(a) at the far right of the particle, while the beginning stages of crack growth can be seen in Figure 4.5(b). As the electrode is cyclically loaded, the crack grows progressively larger, until complete failure is observed in Figure 4.5(d) after the

$10th$ and final cycle. The contours in Figure 4.5 show the relative magnitude of the von-Mises stress within the particle, where the maximum stress level (red) corresponds to the failure initiation stress of the cohesive elements, while the minimum level (blue) corresponds to zero stress. The stress states around the defects in Figure 4.5 are the typical stress profiles around a crack tip, and upon crack advance, the stress within the particle is relaxed in the regions adjacent to the propagated cracks.

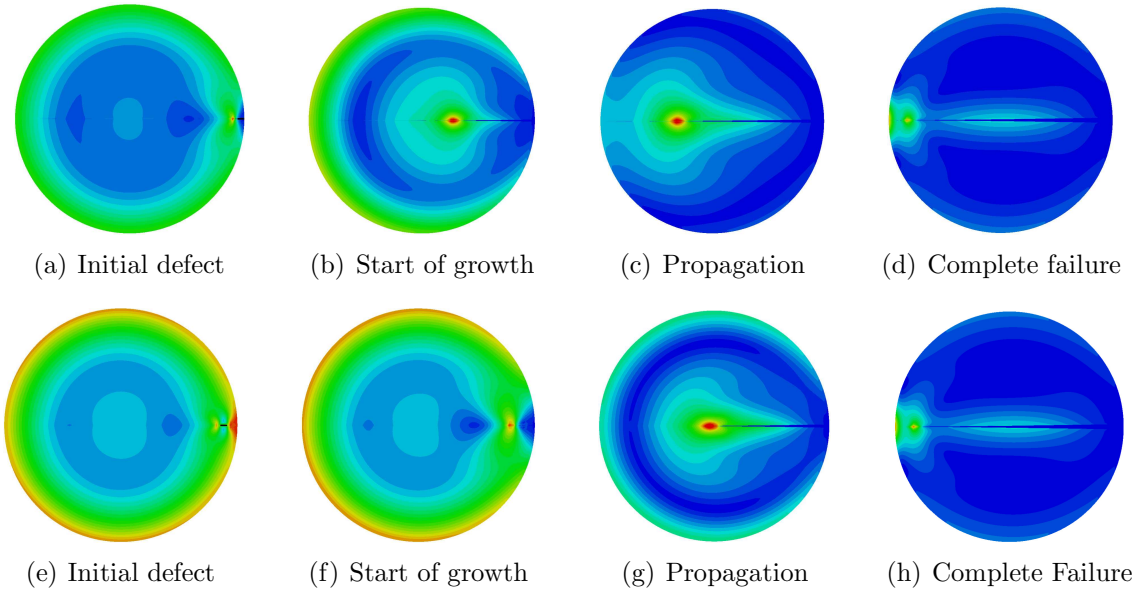

(a) Initial defect (b) Start of growth (c) Propagation (d) Complete failure

(e) Initial defect (f) Start of growth (g) Propagation (h) Complete Failure

Figure 4.5: Crack propagation sequences for radially aligned defects located at the periphery of the particle (a-d), and embedded close to the surface (but still within) of the particle (e-h). The contours show the von-Mises stress within the material, with the maximum level (red) corresponding to the cohesive damage initiation stress, while the minimum level (blue) corresponds to zero stress.

The same sequence is shown in Figures 4.5(e)-4.5(h) for a radially-aligned defect embedded very close to the outer surface of the particle. In the case of an embedded defect, growth begins at the right crack-tip until it reaches the surface of the particle, thereby creating a larger peripheral crack (shown in Figure 4.5(f)); at this point, growth proceeds from the left crack-tip ((Figure 4.5(g)) and continues during cyclic loading, until complete failure of the particle (Figure 4.5(h)). The initial stages of

crack propagation for the defects shown in Figure 4.5 all occur during the delithiation phase of the charging cycle.

The early stages of crack growth for the radially-aligned embedded crack corresponding to Figures 4.5(e)-4.5(g) are shown schematically in Figures 4.6(a)-4.6(c). A defect of length a is embedded a distance d away from the surface of the particle (Figure 4.6(a)). Due to the large hoop stress, the right crack-tip advances to the surface of the particle, creating a new peripheral crack of length $a + d$ (Figure 4.6(b)). Now, the crack proceeds to grow from the left crack-tip, and progressively advances during the subsequent loading cycles (Figure 4.6(c)). Within the notation we have used in this schematic, the length of the peripheral defect in Figure 4.5(a) is a, and so once the embedded crack of Figure 4.5(e) reaches the surface, its stress-intensity factor will be higher than that of the original surface defect due to its longer length of $a + d$.

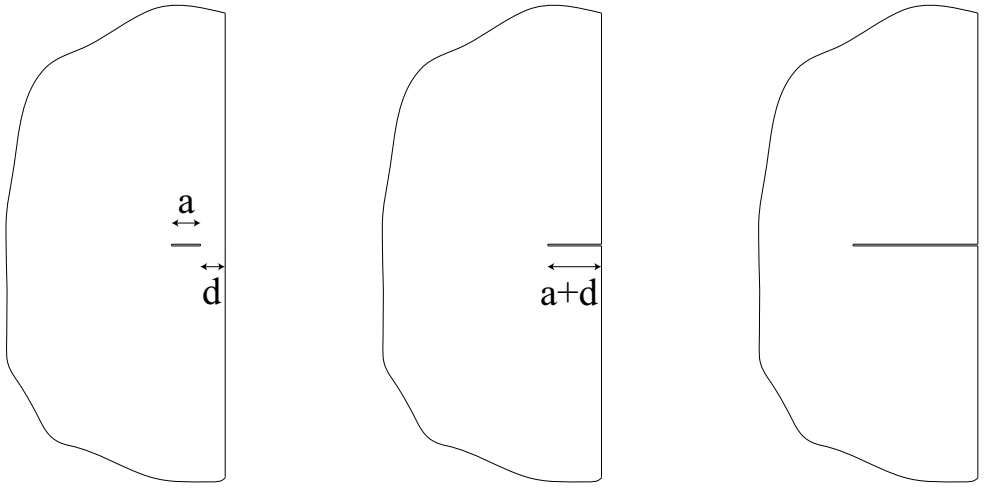

(a) Embedded crack

(b) Growth to the right

(c) Growth to the left

Figure 4.6: Schematic of crack propagation of an embedded crack close to a surface.

The propagation sequence for a radially mis-oriented defect at the periphery of the particle is shown in a Figure 4.7. The characteristics of crack growth for this

case are similar to those of the radially aligned peripheral crack shown in Figures 4.5(a)-4.5(d).

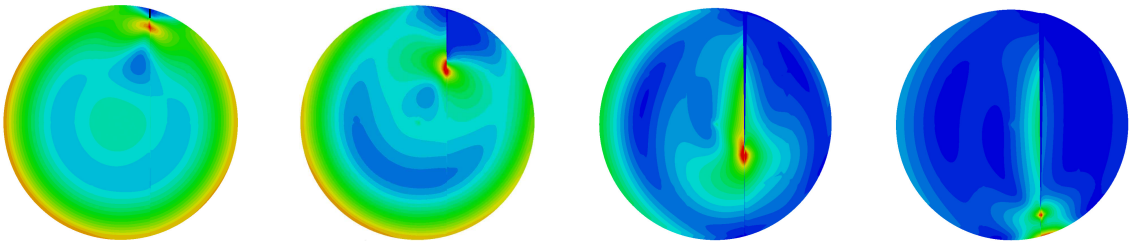

(a) Initial defect (b) Start of growth (c) Propagation (d) Complete failure

Figure 4.7: Crack propagation sequence for a mis-aligned defect located at the periphery of the particle. The contours show the von-Mises stress within the material, with the maximum level (red) corresponding to the cohesive damage initiation stress, while the minimum level (blue) corresponds to zero stress.

4.3.2 Non-Propagating Cracks

As the initial defects move closer to the center of the particle and/or the degree of mis-alignment increases, a threshold is eventually crossed beyond which initial defects transition from unstable to stable and do not propagate, even after repeated cycling. Figures 4.8(a) and 4.8(b) show an example of a stable, radially aligned embedded defect during the delithiation phase of the first and last charging cycles, respectively; the same is shown in Figures 4.8(c) and 4.8(d) for a stable, radially mis-oriented peripheral crack. For both cases, it is clear that the initial defects have not grown during the 10 charging cycles. Our goal henceforth is to explain this phenomenon and identify the boundary separating the stable and unstable regimes.

4.3.3 Stress During Cyclic Loading

The maximum stress far from the defects during the lithiation and delithiation phases of the charging cycle is shown in Figure 4.9. The important stress component

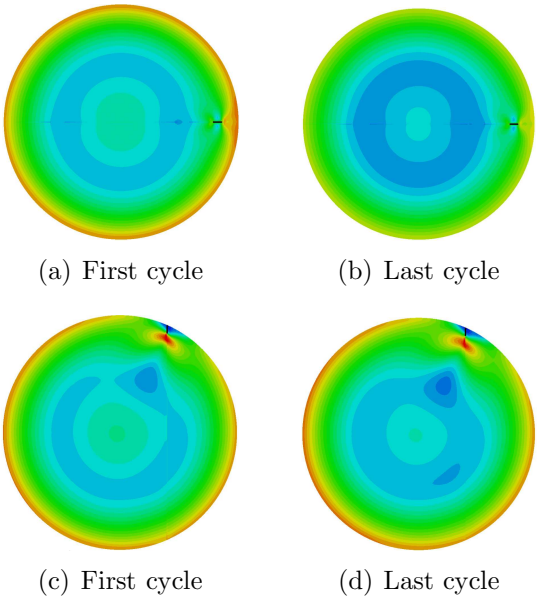

(a) First cycle (b) Last cycle

(c) First cycle (d) Last cycle

Figure 4.8: Examples of stable, non-propagating radial (a,b), and mis-aligned (c,d) defects on the first and last delithiation cycles. The contours show the von-Mises stress within the material, with the maximum level (red) corresponding to the cohesive damage initiation stress, while the minimum level (blue) corresponds to zero stress.

to consider with regards to crack growth is the hoop stress, since it acts perpendicular to radially aligned cracks, placing them under mode I loading. In contrast, radial stress plays no role in advancing radially aligned defects.

During the lithiation phase, lithium diffuses into the outer portions of the particle, leading to compressive hoop stress in these regions. At the same time, since the lithium has not diffused to the center regions of the particle, the compression in the outer regions is counteracted by tensile hoop stress in the region close to the center. Furthermore, due to the radial strain in the outer regions of the particle, the radial stress in the center region is tensile, and decays to zero at the surface of the particle. The stresses during the delithiation phase are virtually a mirror image of those during the lithiation phase. Now, as lithium diffuses out of the particle, the outer regions are placed under tensile hoop stress, while the center regions experience compressive hoop stress.

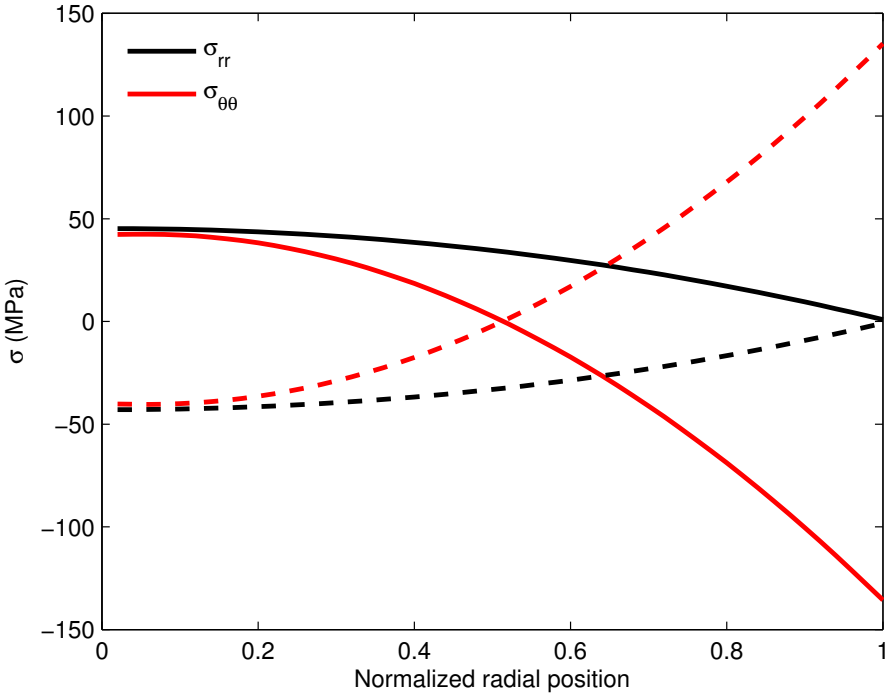

Figure 4.9: The stress distribution along the radius of the particle far from the defect. The solid lines represent the stresses during the lithiation phase, while the dotted lines represent the delithiation phase. Positive stresses are tensile, while negative stresses are compressive. The normalized radial position ranges from the center of the particle (normalized position of 0) to the surface of the particle (normalized position of 1).

As we have mentioned above, radially-aligned defects close to the outer surface of the particle initially propagate during the delithiation phase of the charging cycle only. This phenomenon is due to the high tensile hoop stress in this region; it is clearly impossible to propagate a crack at the surface during lithiation due to the high compressive stress. However, once the crack has grown such that the crack tip lies within the center region of the particle, the lower tensile hoop stress during lithiation can now advance the crack further upon subsequent cycling.

As a radially-aligned initial defect moves closer to the center, the hoop stress acting upon it decreases, as shown in Figure 4.9; once the defect experiences stress below a certain critical level, it becomes stable and no longer propagates. A radially-aligned

defect close to the center of the particle will experience tensile hoop stress during the lithiation phase, however, the magnitude of this stress is too low to initiate crack growth, and so a threshold location exists beyond which defects will not propagate.

In the case of mis-aligned defects, both $\sigma_{\theta\theta}$ and σ_{rr} can contribute to crack propagation depending on how these stresses transform along the direction of the defect. We have plotted a simple stress transformation for a mis-aligned defect situated at the surface of the particle (where σ_{rr} is zero) in Figure 4.10. Clearly, as the mis-alignment angle increases, the normal stress acting on the crack decreases, while the shear stress increases from zero to a maximum at an angle of 45°. If the mis-alignment angle increases beyond a certain point, the component of $\sigma_{\theta\theta}$ acting normal to the crack decreases below the threshold required to propagate the crack, thereby rendering the defect stable. Although there will also be a shear component acting along the defect, its value is always too low to cause mode II failure, and so propagation is governed by the component of $\sigma_{\theta\theta}$ and σ_{rr} normal to mis-aligned defects.

4.3.4 Failure Map

We have performed numerous simulations with different initial defect locations and mis-alignment angles in order to determine the thresholds we have mentioned above; the results of these simulations are plotted in Figure 4.11. This failure map plots the location, d (refer to Figure 4.3 for an explanation of these co-ordinates), versus the orientation angle, θ, for all simulations, using a blue marker for stable defects and a red marker for unstable ones. Due to the number of simulations that have been performed very close to the transition from the stable to unstable regimes, we are able to determine the boundary between the safe and unsafe regions of the map. Using this plot, we can see that for a radially aligned defect to propagate, it must be situated at or beyond 88% of the particle's radius; if it is any closer to the

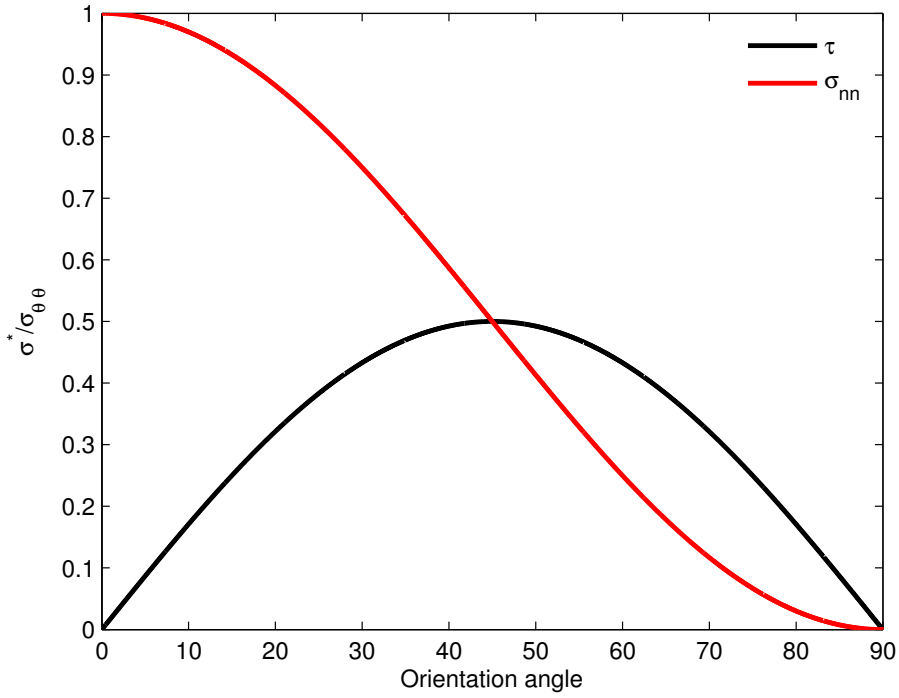

Figure 4.10: Analytical transformation of the hoop stress at the periphery of the particle into normal and shear components along a defect as a function of the mis-alignment angle.

center of the particle, it will not grow. In the case of mis-aligned defects, we can see that any defect with an orientation angle beyond 26° will not grow, no matter where it is situated within the particle. If a defect completely propagates across a particle (or even just to the surface), it will lead to the formation of SEI, which will greatly reduce the capacity of a lithium-ion battery over its lifetime [Aurbach et al. (2002), Zhang, Li, Liu, Tan and Cheng (2005), Liu et al. (2010)]; as a result, the red region of the failure map can be thought of as an indicator of defect locations and orientations that are deleterious to the long-term reliability of lithium-ion batteries.

The size of the failure region shown in Figure 4.11 is directly dependent on some of the model parameters listed in Table 4.1. We will now present a short discussion on the effects of defect length, fracture energy, damage initiation stress, charging period,

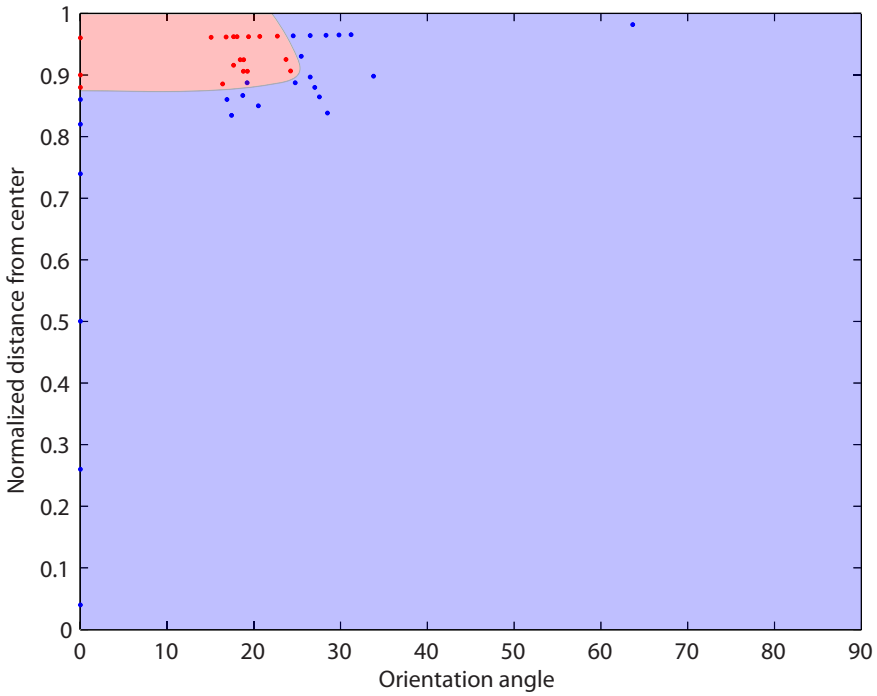

Figure 4.11: A failure map plotting the safe (blue) and unsafe (red) points and regions.

and particle size on the size of the unsafe region of the failure map.

An increase in the length of the original defect, a decrease in the fracture energy, or a decrease in the damage initiation stress, will all increase the size of the failure region. This would mean that defects closer to the center of the particle, and more highly mis-aligned relative to the radial direction, will propagate under the same loading. Similarly, a decrease in the defect length, an increase in the damage initiation stress, or an increase in the fracture energy would decrease the size of the failure region; if these latter changes in the parameters are extreme enough, crack propagation will become impossible under the specified loading conditions.

The period of the potentiostatically-controlled charging curve also has a dramatic effect on the size of the failure region. In order to study the effect of charging rate, we have performed several calculations with radial cracks loaded at different rates.

Figure 4.12 shows the results of analyses performed at $20.0C$, $14.4C$, $13.1C$, and $12.0C$. In this plot, blue points represent initial defect locations that do not lead to failure, while red points are for unsafe locations. At a rate of $20.0C$, defects situated at slightly less than 80% of the particle's radius lead to failure, while at $12.0C$, even a peripheral defect does not propagate. Based on these results, it is evident that as the charging rate increases, defects situated closer to the center of the particle will lead to failure, and it can be inferred that the overall size of the failure region shown in Figure 4.11 will increase with increasing charging rate. This is a consequence of the direct relationship between strain and concentration; larger concentration gradients stemming from faster charging produce larger strain gradients, which in turn lead to higher stress. This result is consistent with the findings of Zhao et al. (2010), who have also found that faster charging leads to larger stress within electrodes.

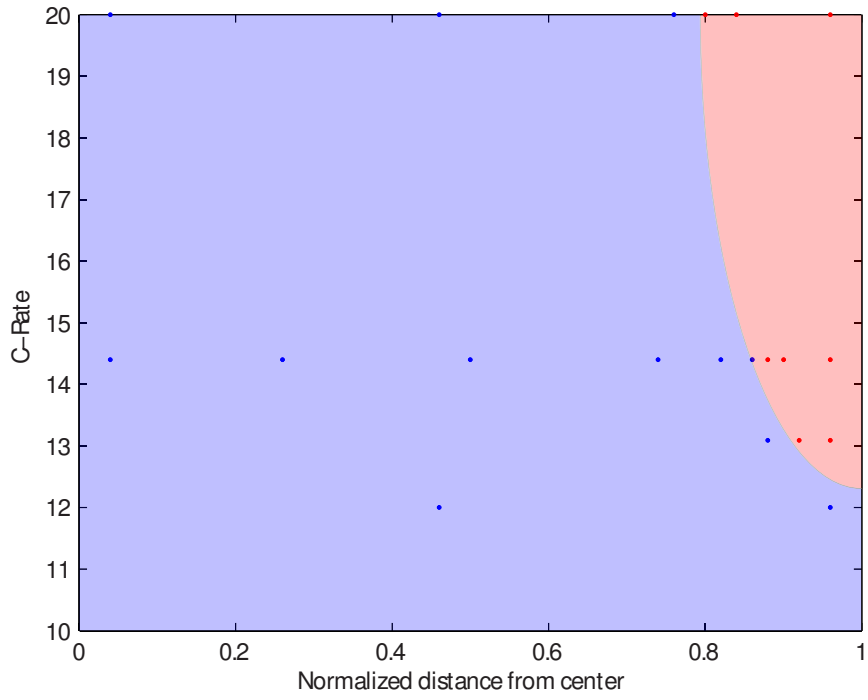

Figure 4.12: A plot showing the effect of charging rate on the failure of defects. Blue regions represent safe locations, while red regions represent progressive failure.

Particle size only has an effect relative to the size of the defect and the charging period. In order to analyze the former effect, we can define a dimensionless length-scale, $\psi = R/a$, where R is the radius of the particle, and a is the length of the defect. As the value of ψ increases - either through an increase in the particle radius or a decrease in the defect length, or both - the size of the failure region will decrease. Similarly, we can define a dimensionless time-scale, $\lambda = R^2/\omega D$, where R is the radius of the particle, ω is the charging period, and D is the diffusion constant. In this case, as λ increases - either through an increase in the particle radius, or a decrease in the charging period, or both - the size of the failure region will increase. This means that if the particle radius and defect size are doubled while the charging period is quadrupled, the values of ψ and λ will remain fixed, and the failure map will not change. The dimensional analysis of the rate effect is consistent with the results presented in Figure 4.12.

4.3.5 Effect of Anisotropy

All the results presented so far have been based on simulations using isotropic material properties. Now, we will present results that were obtained using fully anisotropic diffusion, expansion, and elasticity. The anisotropic diffusion constants lead to much faster lithium diffusion in the direction parallel to the graphene sheets as opposed to the perpendicular direction, as shown by examination of the values presented in Table 4.2. Upon LiC_6 formation, the inter-layer spacing between adjacent graphene sheets increases, which is accounted for in the expansion coefficient perpendicular to the graphene planes, with zero in-plane expansion. The in-plane Young's moduli of graphene (represented by C_{1111} and C_{3333} in Table 4.2) are much greater than the Young's modulus of graphite in the graphene stacking direction (C_{2222}). It is well-known that the shear moduli of graphite (C_{1212}, C_{1313}, C_{2323}) are quite low,

and this fact is also shown in the values presented in Table 4.2.

For the anisotropic analyses, we only considered radially aligned defects for simplicity. The crack propagation sequence for a radially-aligned defect at the periphery of a particle modeled using anisotropic properties is shown in Figures 4.13(a)-4.13(d). The initial defect can be seen on the far right of the particle in Figure 4.13(a), and it begins to grow and propagate in Figures 4.13(b) and 4.13(c), respectively, until it reaches the center of the particle in Figure 4.13(d). Due to the way in which the particle is divided into five segments, the crack cannot progress any further than the center, since it would have to change directions in order to do so. This failure sequence is very similar to the ones shown in Figure 4.5, although the stress contours are much more complicated due to the anisotropic material properties.

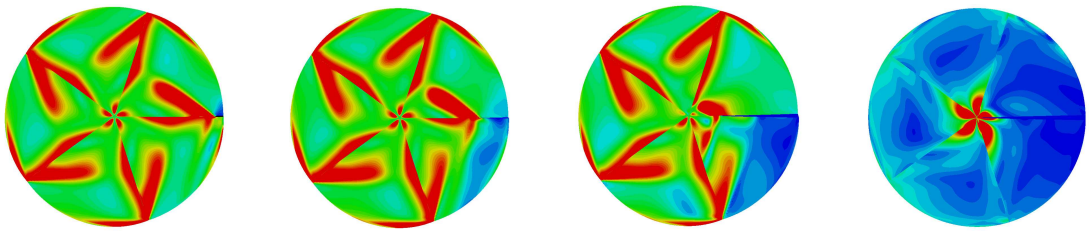

(a) Initial defect (b) Start of growth (c) Propagation (d) Failure

Figure 4.13: Crack propagation sequences for a radially aligned defect located at the periphery of the particle using fully anisotropic diffusion, expansion, and elasticity. The contours show the von-Mises stress within the material, with the maximum level (red) corresponding to the cohesive damage initiation stress, while the minimum level (blue) corresponds to zero stress.

When anisotropy is considered, we once again discover that a threshold location exists beyond which the initial defect no longer propagates, as was the case with the isotropic cases. Figures 4.14(a) and 4.14(b) show an example of a stable, radially aligned embedded defect during the delithiation phase of the first and last charging cycles, respectively. It is clear that the initial defect has not grown during the 10 charging cycles. We have found that for the anisotropic case we have considered, the

critical location that demarcates the safe and unsafe regions is a normalized radial position of 80%. Although we have only considered one anisotropic case, we can see that the qualitative trend is the same as the isotropic case: as the location of the initial defect shifts closer to the center of the particle, the possibility of crack growth decreases. Clearly, due to the highly anisotropic properties of graphite, different material orientations may have a large influence on the details of crack propagation, but such considerations are beyond the scope of this thesis.

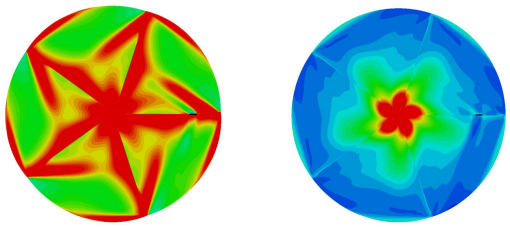

(a) First cycle (b) Last cycle

Figure 4.14: A stable, non-propagating radial defect on the first and last delithiation cycles using fully anisotropic diffusion, expansion, and elasticity. The contours show the von-Mises stress within the material, with the maximum level (red) corresponding to the cohesive damage initiation stress, while the minimum level (blue) corresponds to zero stress.

4.4 Summary

We have used finite element calculations to study the location- and orientation-dependent progressive propagation of defects in cylindrical electrode particles subjected to potentiostatically-controlled cyclic charging. Defects situated close to the boundary of the particle begin to grow during the delithiation phase of the charging cycle, due to the large tensile hoop stress that is generated in that region during lithium de-intercalation. For a defect to grow, it must be far enough from the center of the particle to be subjected to high tensile hoop stress, and must not be too misaligned relative to the radial direction in order for the components of stress normal

to the defect to be large enough to initiate failure. We have used our simulations to construct a failure map demarcating safe and unsafe regions as a function of defect position and orientation. The failure map shows that radially aligned defects will not grow if they are located within 88% of the particle's radius from the center. Defects that are mis-aligned from radial lines by more than 26° are also stable and will not grow, regardless of their location. The influence of particle size, crack microstructure, and charging rate on the failure map is discussed. We have also studied the effects of fully anisotropic behavior, and found that qualitatively, the results pertaining to location-dependent failure are the same as those obtained using an isotropic assumption.

Chapter 5

Fracture in Silicon Nanowire Electrodes

5.1 Introduction

Recently, silicon has garnered a great deal of attention as a possible electrode material for lithium-ion batteries due to its extremely high theoretical capacity (3600 mAh/g, compared to 370 mAh/g for graphite) [Obrovac and Christensen (2004), Chan et al. (2009), Shenoy et al. (2010), Ryu et al. (2011), Magasinski et al. (2010), Kim et al. (2008)]. The use of silicon as an electrode material in lithium-ion batteries has been demonstrated in a number of different particle geometries: Obrovac and Krause (2007) have cyclically lithiated and delithiated silicon powder; Magasinski et al. (2010) have synthesized silicon spheres for use in anodes; Chan et al. (2008), Song et al. (2010), and McDowell et al. (2011) have all developed methods to manufacture silicon nanowires which they have cyclically intercalated with lithium in experiments.

During lithiation, Li_xSi compounds form which cause a large volumetric expansion

- up to nearly 400% - due to the fact that one silicon atom can theoretically bond with a maximum of 3.75 lithium atoms [Obrovac and Christensen (2004)]. This is the source of the major challenge associated with using silicon as an electrode material since it causes large diffusion-induced stresses within the electrodes (much higher than in graphite which only undergoes a 10% increase in volume), which can lead to cracking and a reduction in the capacity of the batteries [Ryu et al. (2011)].

Diffusion-induced stresses during lithiation have been studied by a number of research groups [Zhang et al. (2007), Zhang, Sastry and Shyy (2008), Cheng and Verbrugge (2009), Christensen and Newman (2006)]. In addition to simply studying the stress-states, Cheng and Verbrugge (2010*a*) and Woodford et al. (2010) have developed approximate analytical models for studying fracture in electrodes, while more accurate methods have been presented by Zhao et al. (2010) and Bhandakkar and Gao (2010). In the previous chapter, we have used coupled diffusion-stress finite element calculations to model progressive crack propagation in graphite electrode anodes.

These studies were all performed on materials undergoing small volumetric expansions and their methods are not suitable for studying diffusion-induced stresses in silicon particles. Due to the huge volumetric expansions, the pressure-gradients within silicon become large and affect lithium diffusion. The previously mentioned studies assume that diffusion is simply driven by gradients in concentration, and neglect the effects of the pressure-gradients. Recently, Ryu et al. (2011) have performed finite element analyses of fracture in silicon nanowires with preexisting cracks, and have developed a semi-analytical approach to account for the effects of the pressure-gradients on lithium diffusion. They have done this by analytically solving for the pressure distribution in a cylinder without a crack as a function of concentration, then used this result to redefine the diffusion constant as a function of lithium concentration. They

have performed finite element calculations using the concentration-dependent diffusion constant and computed the J-integral around cracks to determine whether they will grow. In this manner, they have found a simple way to calculate the diffusive flux as a function of the pressure- and concentration-gradients; however, the analytical calculation upon which this method is based ignores the presence of a crack, and is therefore only valid *far away from the crack-tip*. Locally, the crack-tip represents a region of large pressure-gradients and has an important contribution to the local flux, which cannot be accounted for using the methods outlined by Ryu et al. (2011).

In this chapter, we present a method that we have developed to calculate the pressure-gradient effects that allows for a direct coupling between the stress and diffusion solutions. Our method also consists of finite element simulations of silicon nanowires with preexisting cracks; however, instead of analytically redefining the diffusion constant, we numerically calculate the pressure-gradients at each instant and use them along with the concentration gradients to directly calculate the flux vector. We also make use of cohesive finite elements to model fracture as opposed to computing the J-integral, which allows us to observe the growth of cracks during lithiation. Using this approach, we can capture the effect of the crack-tip on the localized diffusive flux. We have used this method to study the relationship between charging rate and nanowire diameter on the fracture of silicon nanowires.

5.2 Computational Methods

5.2.1 Governing Flux and Diffusion Equations

The general diffusion/heat equation has the following form [Smith (2004)]:

$$\frac{\partial \phi}{\partial t} = -\nabla \cdot J \tag{5.1}$$

Here, ϕ represents concentration (or temperature in the heat equation), and J represents the diffusive (or thermal) flux. In most cases, the flux is simply proportional to the concentration (or temperature) gradient, and is given by the standard form of Fick's law [Smith (2004)]:

$$J_F = -D\nabla\phi \tag{5.2}$$

In this equation, D is the diffusion constant of the material (or the thermal diffusivity in the heat equation). In studying the diffusion-induced stresses in silicon - which can experience almost 400% volumetric expansion [Shenoy et al. (2010), Ryu et al. (2011)] upon full lithiation - we must also consider the contributions to the flux from the gradients in pressure. When considering materials such as graphite, which undergo small volumetric expansions, the contributions of the pressure-gradients to the flux are generally ignored; for silicon, however, such an omission is not accurate. The following paragraphs will outline the necessary changes to the governing equations in order to account for the pressure-gradient terms.

The strain in a lithiated material can be decomposed into two parts, the first being an elastic component of strain, and the second being a stress-free strain due to the volumetric expansion caused by lithiation:

$$\epsilon_{ij} = \epsilon_{ij}^E + \frac{\Omega}{3}\phi\delta_{ij} \tag{5.3}$$

Here, Ω represents the volumetric expansion coefficient of the material, and δ_{ij} is simply the Kronecker delta. Based on this equation, the total elastic energy of the material is a function of concentration, therefore an additional elastic contribution term of the following form must be added to the total chemical potential [McDowell et al. (2011)]:

$$\mu_E = -\frac{\Omega}{3}\sigma_{kk} \tag{5.4}$$

In general, flux is related to the gradient of the chemical potential by the following equation [Smith (2004)]:

$$J = -\frac{D}{RT}\phi\nabla\mu \tag{5.5}$$

Substituting Eq. 5.4 into Eq. 5.5 and using the relationship between pressure and the trace of the stress tensor ($P = -\sigma_{kk}/3$), we arrive at the following expression for the pressure-gradient contribution to the diffusive flux:

$$J_P = -\frac{D\Omega\phi}{RT}\nabla P \tag{5.6}$$

Now, we can compute the total flux as a sum of the flux given by the standard form of Fick's law (J_F given in Eq. 5.2), and the pressure-gradient-induced component of the flux (J_P) computed above:

$$J = -D\Big(\nabla\phi + \frac{\Omega\phi}{RT}\nabla P\Big) \tag{5.7}$$

Substituting the above flux into the general diffusion equation given in Eq. 5.1, we arrive at the final governing diffusion equation (with a constant value for D):

$$\frac{\partial\phi}{\partial t} = D\Big[\nabla^2\phi + \frac{\Omega}{RT}\Big(\nabla\phi\cdot\nabla P + \phi\nabla^2 P\Big)\Big] \tag{5.8}$$

Due to the fact that the governing equation contains both concentration and pressure gradients and Laplacians, it must be solved using a coupled diffusion-stress analysis. We have solved this problem using the commercial finite element program,

ABAQUS [ABAQUS Manual (2010)] in conjunction with a user-programmed subroutine. Without an additional user-defined subroutine, ABAQUS is only capable of solving the coupled diffusion-stress problem with the standard form of Fick's law outlined in Eq. 5.2, not the form of the flux given in Eq. 5.7 that incorporates the effects of the pressure-gradients. The following section outlines the methods used in the user-subroutine to numerically calculate the pressure-gradients in order to define the correct diffusive flux.

5.2.2 Numerical Calculation of the Pressure Gradients

We solve the coupled diffusion-stress problem incrementally in time using ABAQUS. In order to calculate the pressure-gradients at time-step i, we use the nodal-averaged (since pressure is computed at integration points, not nodes) pressure results from time-step $i-1$. Due to this backwards-looking scheme, we adopt a small time-step analogous to one used in explicit analyses:

$$\Delta t < \frac{L^2}{D} \tag{5.9}$$

In the above expression, L is the smallest element length, and D is the diffusion constant of the material. Knowing the calculated nodal-averaged pressures and deformed coordinates of the nodes from the previous time-step, we can compute the pressure-gradients at the integration points of each element using the derivatives of the shape functions (the Einstein summation notation is implied):

$$\frac{\partial P}{\partial x_j} = \left(P_r \frac{\partial N_r}{\partial \zeta_k}\right)\left(X_{km} \frac{\partial N_m}{\partial \zeta_j}\right)^{-1} \tag{5.10}$$

Here, P_m is a 4-vector containing the nodal-averaged pressures of each of the 4 nodes of an element (only 4-noded elements were used in our analyses), X_{km} is a

2×4 matrix containing the deformed coordinates (only x and y components, since the models are 2-D axisymmetric) of each node of an element, and $\frac{\partial N_r}{\partial \zeta_k}$ and $\frac{\partial N_m}{\partial \zeta_j}$ are 4×2 matrices listing the derivatives of the bi-linear shape functions. Using the above equation, we can compute the pressure-gradient at each of the 4 integrations points of an element, and use it to compute the total flux given by Eq. 5.7. It should be noted that the concentration gradients are already computed internally by ABAQUS, and are therefore not a part of the user-programmed subroutines.

5.2.3 Coupled Diffusion-Stress Analysis

Once the framework for the calculation of the pressure-gradient-induced flux was established, in order to facilitate the diffusion-stress coupling, we reformulated the diffusion equation to an equivalent heat equation (which requires nothing other than replacing concentration with temperature) and performed a fully coupled thermal-stress analysis instead.

As lithium diffuses into the nanowire, it bonds with silicon and forms $Li_{15}Si_4$, which results in an extreme volumetric expansion of almost 400%. This volumetric expansion drives stress evolution within the nanowire, and is modeled using the same equivalent thermal expansion method as outlined in Section 4.2.2.

The silicon electrode particle was modeled as an axisymmetric cylinder (wire) with a prescribed variation of lithium concentration at its periphery; the concentration was increased from zero to the maximum lithium concentration using a sinusoidal curve. The bottom of the nanowire was constrained from displacement along its axis, however, it was free to move along its radius (corresponding to the nanowire standing on a soft substrate). The cylinder was discretized using 5 nm square axisymmetric elements. Since silicon has recently been shown to undergo plastic deformation, we have modeled plasticity within the nanowire using a von-Mises yield criterion. In

order to study crack propagation in the silicon nanowires, we adopted the same setup as Ryu et al. (2011) and assumed the pre-existence of penny-shaped (axisymmetric) cracks at the center of the wire.

Crack propagation within the nanowires was modeled using cohesive zone elements, which have been outlined in detail in Section 4.2.2. The defects within the silicon nanowires were modeled by assigning a value of zero to the damage initiation stress of the cohesive elements corresponding to the penny-shaped cracks. In this way, at the onset of the slightest tensile stress within the material, these weak regions fail, thereby creating a small initial crack.

All numerical parameters used in our simulations are listed in Table 5.1. We have studied four nanowire diameters with a large range of different charging rates. In our simulations, we have adopted potentiostatically-controlled charging [Cheng and Verbrugge (2009)], where the charging rate refers to half the period of the sinusoidally varying concentration at the surface of the particle (for example, $1C$ means that the lithium concentration is increased from zero to its maximum value in 1 hour), while the maximum concentration refers to the amplitude of this curve. The maximum concentration corresponds to the maximum possible volumetric expansion of silicon during lithium intercalation. The elastic modulus and Poisson's ratio have been assumed to linearly vary between the two extreme values for pure silicon (Si) and fully lithiated silicon ($Li_{15}Si_4$). The expansion coefficient is the equivalent thermal expansion coefficient (α) used in the stress analysis. In order to compare the results for the different nanowire diameters, the diameters of the initial penny-shaped cracks have been kept at a constant ratio of 20% relative to the nanowire diameter. We have assumed the same fracture energy as that used by Ryu et al. (2011) to define the cohesive law, and the damage initiation stress was chosen in such a way as to allow us to observe crack propagation under the more severe loadings.

Table 5.1: Model parameters

Property	Value
Nanowire diameter	250, 350, 450, 550 nm
Nanowire length	1.0 μm
Diffusion constant (D)	1.0×10^{-12} cm^2/s
Charging rate	$0.75C$ - $40.0C$
Maximum concentration	0.18 mol/cm^3
Elastic modulus	150 GPa (Si), 50 GPa ($Li_{15}Si_4$) [Shenoy et al. (2010)]
Poisson's ratio	0.21 (Si), 0.23 ($Li_{15}Si_4$) [Shenoy et al. (2010)]
Yield stress	2000 MPa [Sethuraman et al. (2010)]
Expansion coefficient (α)	3.2 cm^3/mol
Defect diameter	20% of the particle diameter
Fracture energy	2.0 J/m^2 [Ryu et al. (2011)]
Damage initiation stress	750 MPa
Cohesive stiffness	10000 $GPa/\mu m$

5.3 Results and Discussion

We will begin the presentation of our results with a description of the stress state, and flux and concentration distributions within the silicon nanowire during lithiation. In order to emphasize the significance of the pressure-gradient effects on the stress, flux, concentration, and overall observations, we will compare these results to those obtained when the pressure-gradient terms have been neglected. Finally, we will use our method to develop a diagram that illustrates the effects of nanowire diameter and charging rate on crack propagation and failure.

5.3.1 Stress, Flux, and Concentration During Lithiation

Figure 5.1 shows several stress states within a 350 nm silicon nanowire for the first 150 seconds of lithiation at a charging rate of $3C$ (note that the model is axisymmetric: the right edge is the outer periphery, while the left edge is the central axis of the nanowire). As lithium begins to diffuse into the silicon at the periphery of the

nanowire, the material at the outer region expands, leading to compressive axial stress on the nanowire within the lithiated outer region, and a corresponding tensile axial stress on the inner region which contains the penny-shaped crack. In Figure 5.1(d) we can see a localized region of high stress (red) at the crack tip due to the tensile stress-state caused by the lithiated outer region of the nanowire. At this point, some damage has accumulated at the crack-tip and it has grown slightly. As the lithium diffuses further into the particle, the gradients in strain are diminished, and so the stress begins to decline, as shown in Figures 5.1(e) and 5.1(f). Furthermore, diffusion towards the crack-tip reduces the local tensile stress (we will discuss this phenomenon in more detail later in the chapter). Because of the reduced stress-states, crack-tip damage accumulation ceases, the crack becomes stable, and the nanowire is able to fully lithiate without any further crack growth (we will refer to this type of growth as stable). As we will discuss later, depending on the charging rate, the nanowire may or may not be able to fully lithiate without unstable crack growth causing complete failure (unstable crack growth referring to a crack that would grow across the entire diameter of the nanowire).

The flux distributions corresponding to the stress-states discussed above are shown in Figure 5.2. A concentration gradient at the periphery initially causes the lithium to diffuse into the nanowire, but as the lithiated outer region expands, it also creates a pressure-gradient across the radius of the nanowire, which provides a further driving force for lithium diffusion. After an elapsed time of 60 s (shown in Figure 5.2(c)), we can already begin to see the influence of the crack-tip on mass diffusion; this influence is much more evident after 120 s (Figure 5.2(e)) and 150 s (Figure 5.2(f)), where we can observe a localized region of high mass flux at the crack-tip. As the diffusion-induced stresses increase, a very localized region of high tensile stress forms at the crack-tip. Based on Eq. 5.7, mass flows from regions of high pressure to low

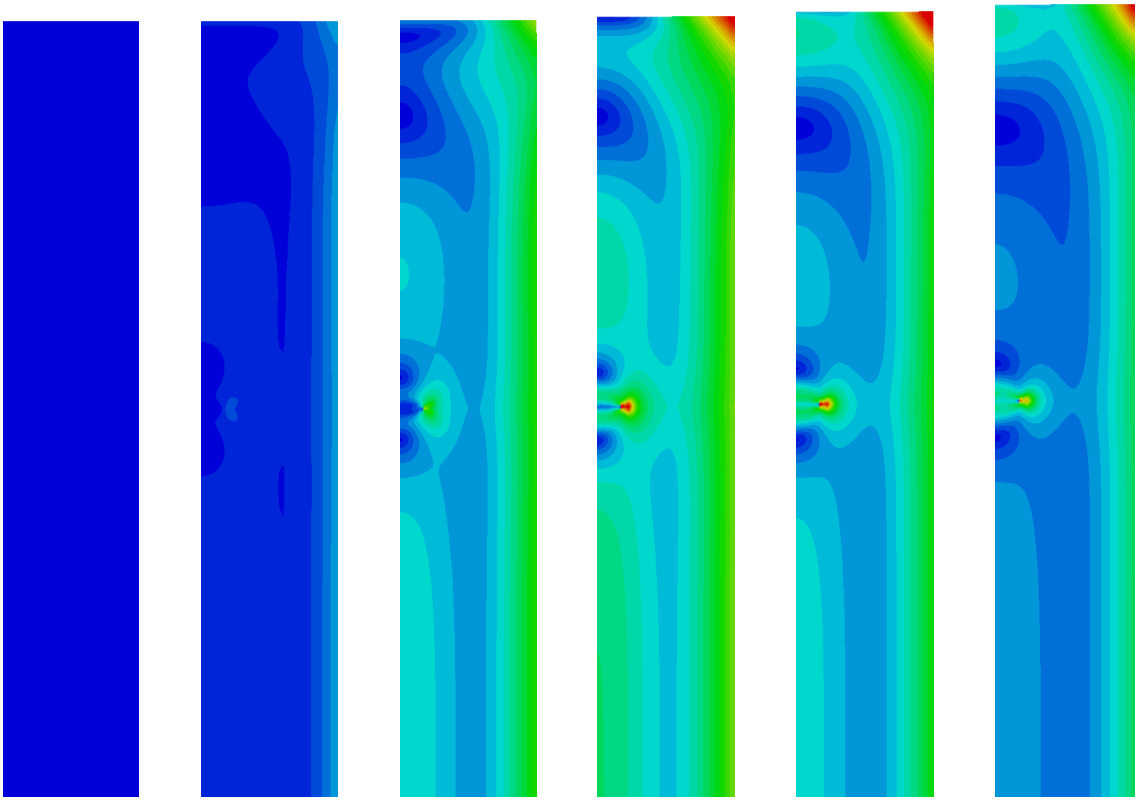

(a) t=0 (b) t=30 s (c) t=60 s (d) t=90 s (e) t=120 s (f) t=150 s

Figure 5.1: Stress contours for a 350 nm nanowire charged at a rate of $3C$ at various times (in seconds) during lithiation. The contours indicate the level of the von-Mises stress within the material, with the lowest level (blue) corresponding to zero and the highest level (red) corresponding to a stress of 500 MPa.

pressure, and since the localized tensile stress represents an area of very low pressure, there is a large mass flux towards the crack-tip.

Localized flux towards the crack-tip has a very important consequence, which is shown schematically in Figure 5.3. In Figure 5.3(a), we have depicted an area of highly-localized tensile stress (the red region) within an otherwise moderately stressed nanowire (the yellow region). The large pressure-gradient between these two regions causes lithium to diffuse towards the crack-tip (the arrows representing the flux). Due to the influx of lithium, the localized area around the crack-tip expands - as depicted in Figure 5.3(b) - which lowers the tensile stress within this region (the reduction

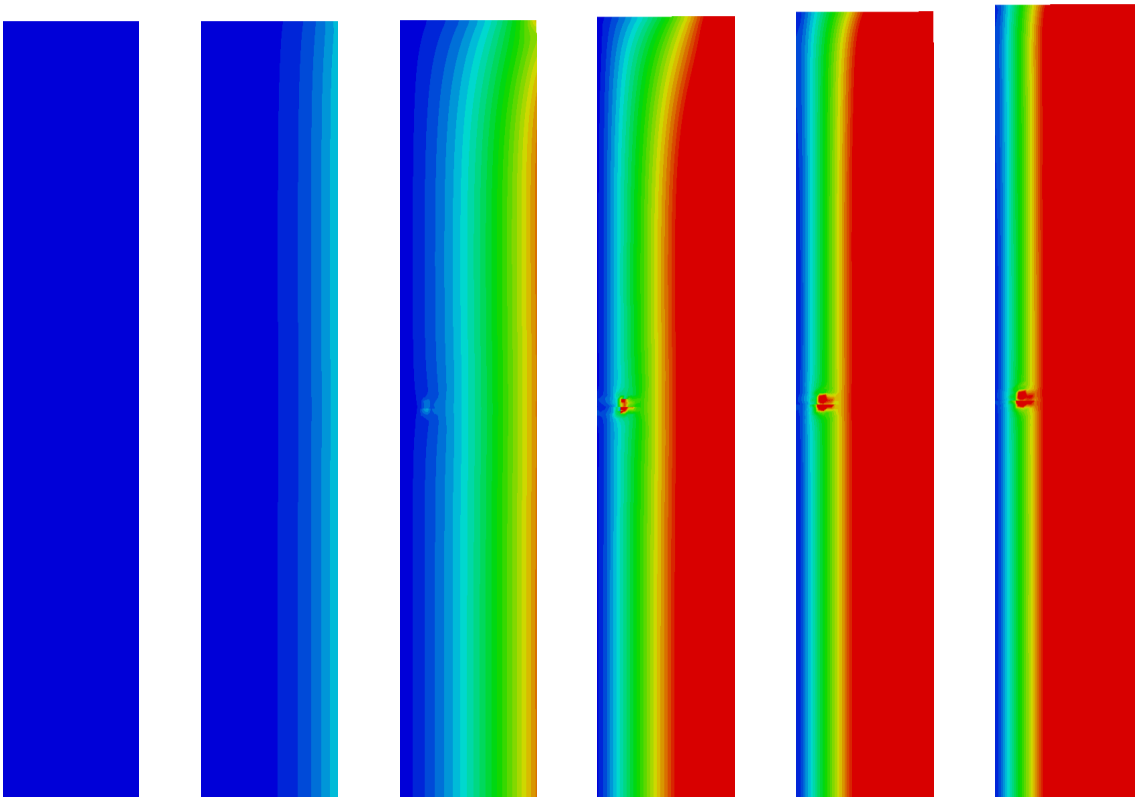

(a) t=0 (b) t=30 s (c) t=60 s (d) t=90 s (e) t=120 s (f) t=150 s

Figure 5.2: Mass flux contours for a 350 nm nanowire charged at a rate of $3C$ at various times (in seconds) during lithiation. The contours indicate the magnitude of the diffusive mass flux within the material, with the lowest level (blue) corresponding to zero and the highest level (red) corresponding to a flux of 3.0×10^{-6} $mol/m^2 s$.

in stress is represented schematically by a change in color from red to orange). The reduction in stress is due to the fact that volumetric expansion causes a stress-free strain, as outlined by the strain decomposition in Eq. 5.3. For a given total strain, ϵ_{ij}, an increase in the strain caused by volumetric expansion, $\frac{\Omega}{3}\phi\delta_{ij}$, will lower the elastic strain, ϵ^E_{ij}, leading to a corresponding decrease in stress. Due to the reduction of the localized stress, lithium diffusion towards the crack-tip can arrest, or at the very least, retard damage accumulation and crack growth.

The concentration profiles at various times during lithiation are shown in Figure 5.4. Clearly, the lithium concentration within the nanowire increases with time, but

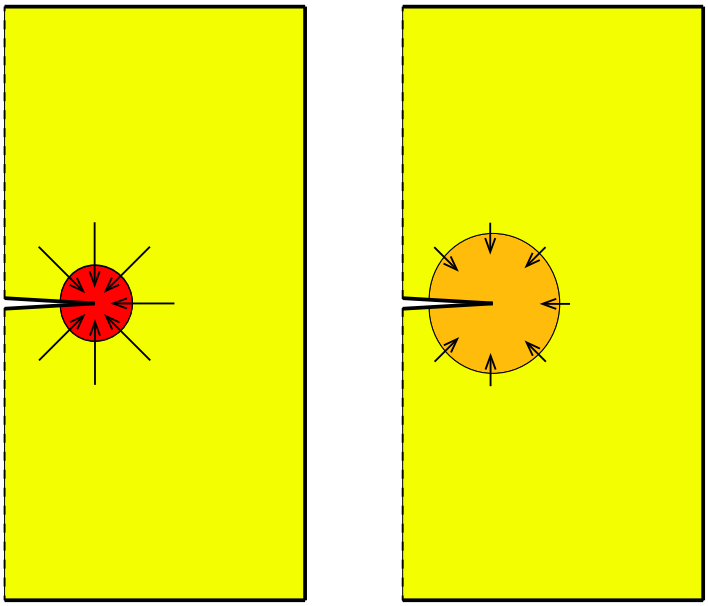

(a) Localized diffusion caused by large ∇P

(b) Reduced localized stress due to volumetric expansion

Figure 5.3: Schematics of the effect of crack-tip diffusion on the localized stress.

what's much more important is the influence of the crack-tip on the concentration. In Figure 5.4(f), we can see a small localized area just to the right of the crack-tip where the concentration is higher than that of the surrounding areas. This is a direct result of the crack-tip diffusion discussed above.

Having examined Figures 5.1, 5.2, and 5.4, we can see how stress, flux, and concentration are interrelated, which is a consequence of the fully-coupled nature of the problem. As lithium diffuses into the material, it causes a volumetric expansion that leads to stress and gradients in pressure. The pressure gradients, along with gradients in concentration, provide the driving force for the mass flux that will further influence the stress-states. In the following section, we will illustrate the results of simulations in which the inherent influence of stress (pressure) on diffusion has been ignored, in order to further explain the role of the pressure-gradients on crack propagation within silicon nanowires.

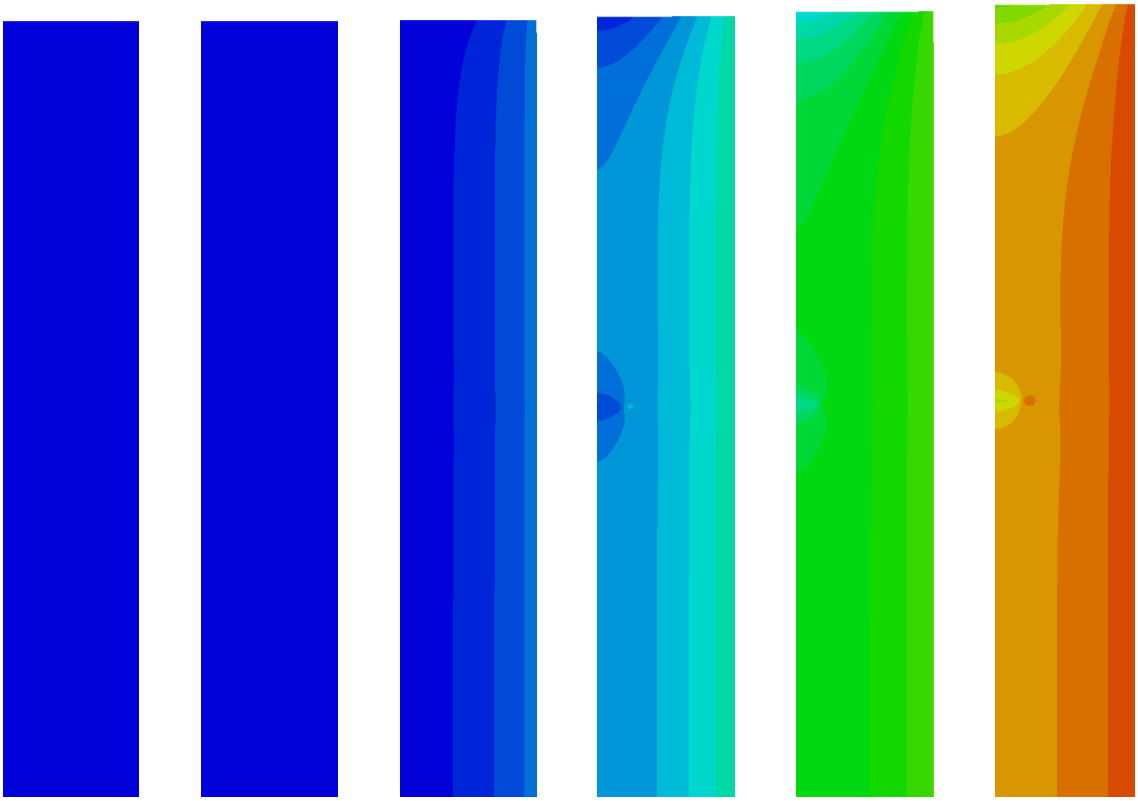

(a) t=0 (b) t=30 s (c) t=60 s (d) t=90 s (e) t=120 s (f) t=150 s

Figure 5.4: Concentration contours for a 350 nm nanowire charged at a rate of $3C$ at various times (in seconds) during lithiation. The contours represent the concentration distribution within the material, with the lowest level (blue) corresponding to zero and the highest level (red) corresponding to a concentration of 7.5×10^{-3} mol/cm^3.

5.3.2 Comparison of Results With and Without the Pressure-Gradient Effects

A juxtaposition of the computed von-Mises stress-states for a 350 nm silicon nanowire charged at $3C$ after 150 seconds of lithiation is shown in Figure 5.5, with and without the pressure-gradient effects. A comparison of stress along the axis of the nanowire (σ_{zz} in cylindrical coordinates) after 90 seconds (roughly corresponding to the time at which σ_{zz} is at its maximum) is also shown in Figure 5.6 close to the crack-tip. The differences between the two results are striking; when the pressure-gradient

effects are ignored, the majority of the material experiences a level of von-Mises stress above 500 MPa (the maximum contour level in Figure 5.5), while the results with the pressure-gradient effects show that the entire nanowire - except at the crack-tip and the top edge - is well below this level. The maximum axial stress (the component of stress that causes crack growth) near the crack is also much lower when considering the pressure-gradient effects, as shown in Figure 5.6. This has a significant effect on the predicted crack propagation results, since the higher predicted stress-levels that are a result of omitting the pressure-gradient terms can cause a crack to grow, whereas in actuality, it would not grow due to the influence of the pressure-gradient effects. For example, when considering the pressure-gradient effects, we have found that a 350 nm diameter nanowire must be charged at $18C$ or higher to cause unstable crack growth, whereas omitting these effects causes complete failure at just $1C$. This difference is a direct consequence of the distinctly different stress-states shown in Figure 5.5, and illustrates the importance of accounting for the pressure-gradient effects on diffusion-induced-stress within silicon.

In order to explain the differences in the stress-states shown in Figures 5.5 and 5.6, we need to examine the diffusive flux within the material in a similar manner - with and without the pressure-gradient effects - which is shown in Figure 5.7. The maximum flux level of 3.0×10^{-6} mol/m^2s (the value corresponding the red contour level) has reached about halfway along the radius of the nanowire when the pressure-gradient terms have been omitted, as opposed to roughly two-thirds when they have been accounted for. This is a direct cause of the gradients in pressure, which increase the magnitude of the flux when compared to the standard form of Fick's law. Higher flux levels lead to a more constant concentration distribution, hence less severe gradients in strain and lower stresses. This explains why the overall stress-states are much lower when considering the pressure-gradient effects. However, another important

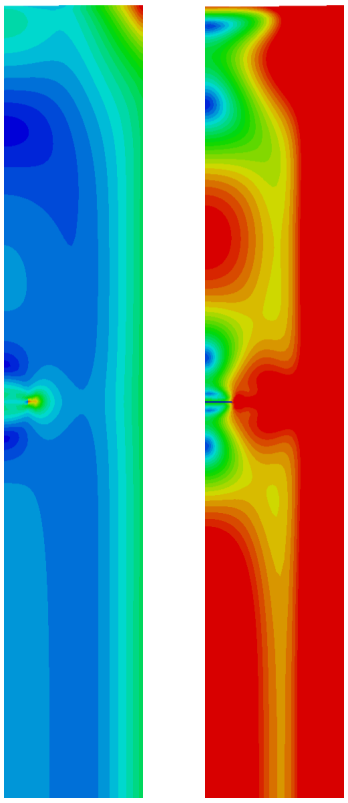

(a) With ∇P (b) Without ∇P

Figure 5.5: Stress contours for a 350 nm nanowire charged at a rate of $3C$, after being lithiated for 150 seconds. The contours indicate the level of von-Mises stress within the material with (a) and without (b) the pressure-gradient effects. The lowest level (blue) corresponds to zero and the highest level (red) corresponds to a stress of 500 MPa.

contribution involves the local phenomenon of diffusion towards the crack-tip. In Figure 5.5(a), we can clearly see a localized area of high flux directly at the crack-tip, which is obviously absent in Figure 5.5(b). This localized flux acts to lower the tensile stress at the crack-tip (due to the resulting volumetric expansion), which reduces the likelihood of unstable crack growth. Even if the tensile stress at the crack-tip is initially high enough to cause damage and growth, depending on the charging rate (this dependence will be discussed in the following section), the diffusion towards the crack-tip may lower the localized stress enough to arrest crack growth and allow the

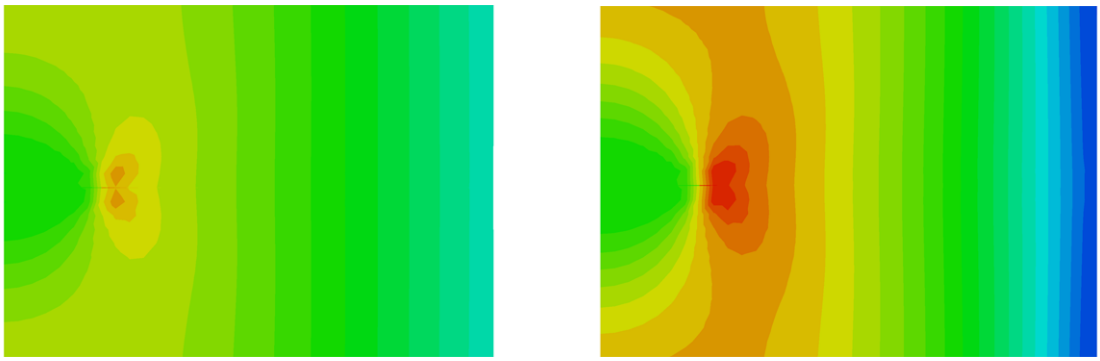

(a) With ∇P (b) Without ∇P

Figure 5.6: Stress contours near the crack-tip for a 350 nm nanowire charged at a rate of $3C$, after being lithiated for 90 seconds. The contours indicate the level of stress along the axis of the nanowire (σ_{zz} in cylindrical coordinates) with (a) and without (b) the pressure-gradient effects. The lowest level (blue) corresponds to a stress of -750 MPa and the highest level (red) corresponds to 750 MPa.

nanowire to fully lithiate without complete failure. The overall higher magnitudes of flux coupled with the crack-tip diffusion explains the above mentioned discrepancy in the charging rates that were predicted to cause unstable crack growth.

Figure 5.8 presents a comparison of the concentration distribution within the material when considering and omitting the pressure-gradient effects. It should come as no surprise at this point that the differences are once again significant. The nanowire has a much higher overall lithium concentration and a much more constant concentration profile when including the pressure-gradient effects, due to the higher flux discussed above. We can also observe the influence of the crack-tip diffusion on the concentration profile when considering the pressure-gradient effects (localized area of higher concentration adjacent to the crack-tip), whereas this phenomenon is impossible to capture when omitting the pressure-gradient terms. The free boundary condition at the top of the nanowire also affects the concentration profile as shown in Figure 5.8(a), which is absent from Figure 5.8(b), although this does not affect crack propagation.

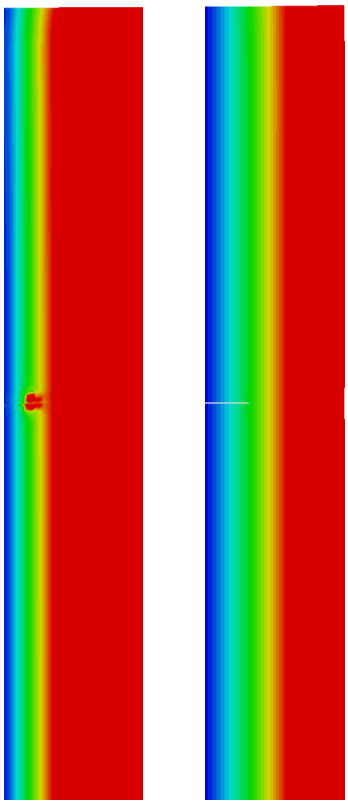

(a) With ∇P (b) Without ∇P

Figure 5.7: Mass flux contours for a 350 nm nanowire charged at a rate of $3C$, after being lithiated for 150 seconds. The contours indicate the magnitude of the diffusive mass flux within the material with (a) and without (b) the pressure-gradient effects. The lowest level (blue) corresponds to zero and the highest level (red) corresponds to a flux of 3.0×10^{-6} $mol/m^2 s$.

Based on the results presented in this section it is evident that in order to study crack propagation in silicon electrodes, the pressure-gradient effects must be accounted for, not only in a global sense as performed by Ryu et al. (2011), but also in a manner that captures the localized diffusion towards the crack-tip. The method used by Ryu et al. (2011) is a semi-analytic method in which the diffusion constant is analytically formulated as a function of concentration, and then used in the numerical simulations. This method will accurately calculate the pressure-gradient contributions to the flux but only *far from the crack-tip*, since the analytical formulation

ignores the presence of a crack. As we have shown, the magnitude of the crack-tip diffusion is significant and plays an important role in arresting crack growth, therefore a method that can account for this local effect must be used when studying cracks in silicon nanowires.

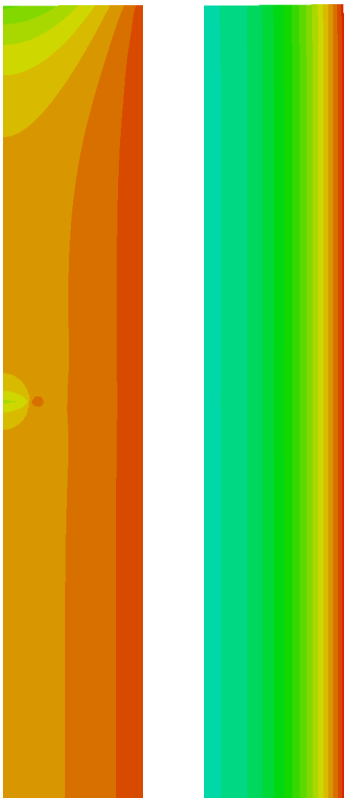

(a) With ∇P (b) Without ∇P

Figure 5.8: Concentration contours for a 350 nm nanowire charged at a rate of $3C$, after being lithiated for 150 seconds. The contours represent the concentration distribution within the material with (a) and without (b) the pressure-gradient effects. The lowest level (blue) corresponds to zero and the highest level (red) corresponds to a concentration of 7.5×10^{-3} mol/cm^3.

5.3.3 Effect of Nanowire Diameter and Charging Rate on Crack Growth

Having established the importance of accounting for the pressure-gradient effects when modeling cracks in silicon nanowires, we now focus our attention on using this method to understand how particle diameter and charging rate affect crack propagation. To this end, we have simulated four different nanowire diameters (250, 350, 450, and 550 nm) at a wide range of charging rates from $0.75C$ - $40.0C$. In all cases, the pre-existing cracks were assumed to have a diameter of 20% relative to the nanowire diameter.

We have observed three distinct types of crack growth in our simulations, which are shown schematically in Figure 5.9. The first type, shown in Figure 5.9(a), corresponds to no growth or damage accumulation during lithiation. Within this regime, a nanowire can be repeatedly charged and discharged without any cyclic crack growth since the stresses during a lithiation cycle are insufficient to cause any growth. The second type, shown in Figure 5.9(b), corresponds to a crack that grows partially across the nanowire but is ultimately arrested during one lithiation cycle. This type of growth can eventually lead to complete failure after a number of cycles, since the crack can move across the radius of the nanowire incrementally with each progressive cycle until reaching the periphery and causing complete failure. The final crack growth regime, shown in Figure 5.9(c), corresponds to unstable crack growth which leads to complete failure in one lithiation cycle.

For each combination of charging rate and nanowire diameter, we have plotted a point on the failure diagram shown in Figure 5.10. The blue points are for combinations that do not lead to any crack growth (represented by Figure 5.9(a)), the yellow points induce some damage and stable growth but are ultimately arrested (Figure 5.9(b)), and the red points designate unstable and complete crack growth (Figure

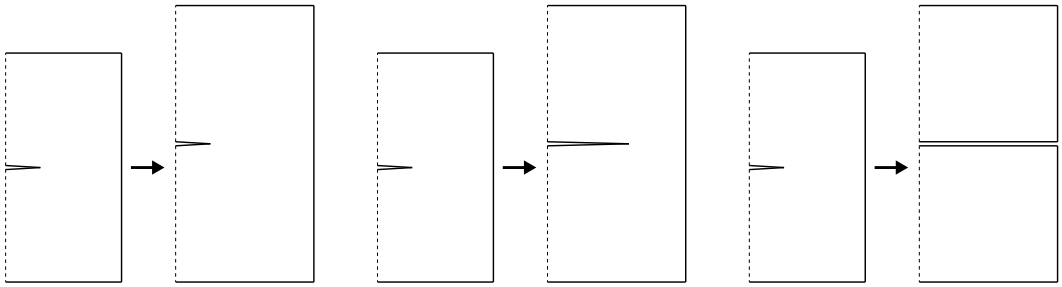

(a) No Growth (b) Arrested Growth (c) Complete Failure

Figure 5.9: Schematics of the three crack growth regimes.

5.9(c)). We have drawn rough boundaries between regions of points to produce the failure diagram.

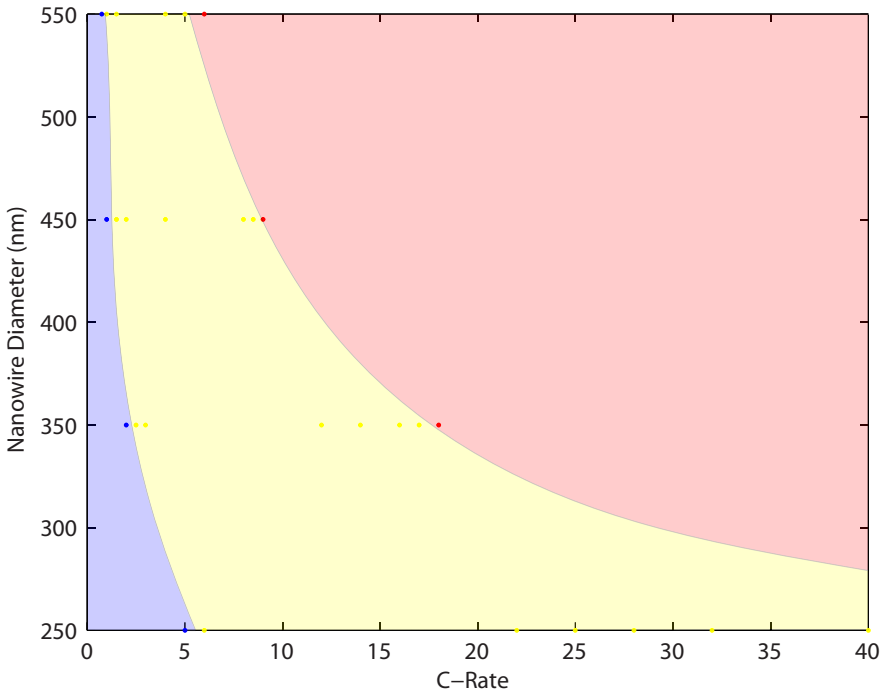

Figure 5.10: A failure diagram illustrating the relationship between charging rate and particle size on crack propagation within silicon nanowire electrodes. Red regions indicate unstable crack growth leading to complete failure, yellow represents regions of stable, arrested crack growth, and blue indicates that the crack does not grow at all and incurs no damage during lithiation.

With the crack sizes we have chosen, in order to charge the nanowire without incurring any crack-tip damage, the charging rates must be low - from $0.75C$ for a 550 nm nanowire to $5.0C$ for a 250 nm nanowire. For complete failure due to unstable crack growth, much higher charging rates are necessary - from $6.0C$ for a 550 nm nanowire to $18.0C$ for a 350 nm nanowire (we did not observe unstable growth in a 250 nm nanowire within our range of charging rates). The wide region separating these two extremes corresponds to stable, arrested growth; for example, for a 350 nm nanowire, the range is from $2.0C$ - $18.0C$, a nine-fold difference.

This wide middle region is mainly a consequence of the crack-tip diffusion we have already discussed; within the yellow region, as the crack begins to grow due to the highly localized tensile stress, the diffusion towards the crack-tip eventually lowers the local stress enough to arrest growth. If the charging rates are within the red region, the stresses are too high and crack-tip diffusion is not sufficient to arrest growth, therefore unstable growth occurs. The increased overall magnitudes of flux due to the global gradients in pressure also contribute to growth arrest, although, it is difficult to assess the degree to which they are responsible.

Although we have drawn the boundaries between the three regions of Figure 5.10 in an approximate manner, we can nevertheless show that their shapes should be parabolic. We can combine the charging time, ω, and the nanowire radius, R, along with the diffusion constant, D, to form a non-dimensional time-scale, $\lambda = R^2/\omega D$. As we have already observed, as the particle radius increases, or the charging time decreases (corresponding to an increase in the charging rate), failure becomes more probable. In both cases, the concentration and strain gradients increase along the radius of the nanowire, which results in higher stresses. This means that as λ increases, the probability of crack growth increases, and due to the dimensions of the diffusion constant, the relationship between particle radius and charging time (or rate) is

parabolic, which is shown by the shape of the boundaries drawn in Figure 5.10.

5.4 Summary

We have used finite element calculations along with user-defined subroutines in order to account for pressure-gradient-induced diffusion when modeling crack propagation in lithiated silicon nanowires containing pre-existing defects. We have found that the pressure-gradient effects significantly affect the flux, not only in a global sense, but also in a localized manner at the crack-tip. Diffusion towards the crack-tip lowers the local tensile stress and can lead to arrested crack growth during lithiation. Simulations which ignore the effects of the pressure-gradients predict drastically different results from those accounting for these effects. We have used our method to examine the effects of charging rate and diameter on crack propagation in silicon nanowires and have found three growth regimes: fast charging rates and/or large diameters cause unstable crack growth; slow charging rates and/or small diameters lead to no damage or growth at all; medium charging rates and/or diameters cause some growth which is ultimately arrested, but can grow further upon subsequent lithiation-delithiation cycling. We have used a simple dimensional analysis to explain why the boundaries between these regimes should be parabolic in shape.

Chapter 6

Conclusions

Using molecular dynamics and finite element simulations, we have addressed fracture in three technologies that may become pervasive in future electronics. We have shown that the intersections between adjacent surface facets of Wurtzite nanowires are a favorable site for crack nucleation. In Zinc-Blende nanowires, the intersections between two opposing surface facets create a stress singularity that facilitates crack nucleation and makes Zinc-Blende nanowires weaker than Wurtzite nanowires.

We have discovered an unusual result when studying the failure of graphene sheets with grain boundaries; as the grain boundary angle increases, the strength of the sheets also increases, a result that cannot be explained using continuum fracture mechanics methods or intuition. The cause of this has been identified as the unstressed length of certain critical carbon-carbon bonds at the grain boundaries.

Using finite element simulations, we have shown that fracture in cylindrical graphite electrode particles is governed by the location and orientation of preexisting defects. In order for a defect to grow during use of a lithium-ion battery, it must be located close to the periphery of the electrode particle and be roughly aligned with the radial direction. In contrast, defects that are close to the center of the particle and/or are highly misaligned with the radial direction will not propagate.

In studying the fracture of silicon nanowire electrodes, we have developed a method within a finite element framework in order to account for the pressure-gradient effects on the diffusion of lithium within silicon. We have found that the pressure-gradients within the material significantly affect the flux, not only in a global sense, but also locally at the crack-tip. Crack-tip diffusion has been identified as an important phenomenon which can arrest crack growth.

Bibliography

ABAQUS Manual, (2010), Dassault Systemes, Providence, RI, Version 6.10.

Aifantis, K. E., Hackney, S. A. and Dempsey, J. P. (2007), 'Design criteria for nanostructured li-ion batteries', *Journal of Power Sources* **165**(2), 874–879.

Albrecht, T., Mizes, H., Nogami, J., Park, S. and Quate, C. (1988), 'Observation of Tilt Boundaries in Graphite by Scanning Tunneling Microscopy and Associated Multiple Tip Effects', *Applied Physics Letters* **52**(5), 362–364.

Algra, R., Verheijen, M., Borgstrom, M., Feiner, L., Immink, G., van Enckevort, W., Vlieg, E. and Bakkers, E. (2008), 'Twinning Superlattices in Indium Phosphide Nanowires', *Nature* **456**(7220), 369–372.

Aurbach, D., Koltypin, M. and Teller, H. (2002), 'In situ afm imaging of surface phenomena on composite graphite electrodes during lithium insertion', *Langmuir* **18**(23), 9000–9009.

Barenblatt, G. I. (1962), 'The mathematical theory of equilibrium cracks in brittle fracture', *Advances in Applied Mechanics* **7**, 56–129.

Basinski, Z., Duesberry, M. and Taylor, R. (1971), 'Influence of shear stress on screw dislocations in a model sodium lattice', *Canadian Journal of Physics* **49**(16), 2160–2180.

Bhandakkar, T. K. and Gao, H. J. (2010), 'Cohesive modeling of crack nucleation under diffusion induced stresses in a thin strip: Implications on the critical size for flaw tolerant battery electrodes', *International Journal of Solids and Structures* **47**(10), 1424–1434.

Blakslee, O. L., Proctor, D. G., Seldin, E. J., Spence, G. B. and Weng, T. (1970), 'Elastic constants of compression-annealed pyrolytic graphite', *Journal of Applied Physics* **41**(8), 3373–3382.

Broberg, K. (1999), *Cracks and Fracture*, Academic Press.

Caroff, P., Dick, K., Johansson, J., Messing, M., Deppert, K. and Samuelson, L. (2009), 'Controlled Polytypic and Twin-Plane Superlattices in III-V Nanowires', *Nature Nanotechnology* **4**(1), 50–55.

Cervenka, J. and Flipse, C. (2009), 'Structural and Electronic Properties of Grain Boundaries in Graphite: Planes of Periodically Distributed Point Defects', *Physical Review B* **79**(19).

Cervenka, J., Katsnelson, M. and Flipse, C. (2009), 'Room-Temperature Ferromagnetism in Graphite Driven by Two-Dimensional Networks of Point Defects', *Nature Physics* **5**(11), 840–844.

Chan, C. K., Peng, H., Liu, G., McIlwrath, K., Zhang, X. F., Huggins, R. A. and Cui, Y. (2008), 'High-Performance Lithium Battery Anodes Using Silicon Nanowires', *Nature Nanotechnology* **3**(1), 31–35.

Chan, C. K., Ruffo, R., Hong, S. S., Huggins, R. A. and Cui, Y. (2009), 'Structural and Electrochemical Study of the Reaction of Lithium with Silicon Nanowires', *Journal of Power Sources* **189**(1), 34–39.

Chandra, N., Namilae, S. and Shet, C. (2004), 'Local elastic properties of carbon nanotubes in the presence of stone-wales defects', *Physical Review B* **69**(9), 094101.

Cheng, Y. T. and Verbrugge, M. W. (2009), 'Evolution of stress within a spherical insertion electrode particle under potentiostatic and galvanostatic operation', *Journal of Power Sources* **190**(2), 453–460.

Cheng, Y. T. and Verbrugge, M. W. (2010*a*), 'Application of hasselman's crack propagation model to insertion electrodes', *Electrochemical and Solid State Letters* **13**(9), A128–A131.

Cheng, Y. T. and Verbrugge, M. W. (2010*b*), 'Diffusion-induced stress, interfacial charge transfer, and criteria for avoiding crack initiation of electrode particles', *Journal of the Electrochemical Society* **157**(4), A508–A516.

Christensen, J. and Newman, J. (2006), 'A Mathematical Model of Stress Generation and Fracture in Lithium Manganese Oxide', *Journal of the Electrochemical Society* **153**(6), A1019–A1030.

Deng, C. and Sansoz, F. (2009), 'Enabling Ultrahigh Plastic Flow and Work Hardening in Twinned Gold Nanowires', *Nano Letters* **9**(4), 1517–1522.

Dick, K., Deppert, K., Larsson, M., Martensson, T., Seifert, W., Wallenberg, L. and Samuelson, L. (2004), 'Synthesis of Branched 'Nanotrees' by Controlled Seeding of Multiple Branching Events', *Nature Materials* **3**(6), 380–384.

Duan, X., Huang, Y., Agarwal, R. and Lieber, C. (2003), 'Single-Nanowire Electrically Driven Lasers', *Nature* **421**(6920), 241–245.

Dugdale, D. S. (1960), 'Yielding of steel sheets containing slits', *Journal of the Mechanics and Physics of Solids* **8**, 100–104.

Geim, A. (2009), 'Graphene: Status and Prospects', *Science* **324**(5934), 1530–1534.

Geim, A. and Novoselov, K. (2007), 'The Rise of Graphene', *Nature Materials* **6**(3), 183–191.

Harris, S. J., Deshpande, R. D., Qi, Y., Dutta, I. and Cheng, Y. T. (2010), 'Mesopores inside electrode particles can change the li-ion transport mechanism and diffusion-induced stress', *Journal of Materials Research* **25**(8), 1433–1440.

Hashimoto, A., Suenaga, K., Gloter, A., Urita, K. and Iijima, S. (2004), 'Direct Evidence for Atomic Defects in Graphene Layers', *Nature* **430**(7002), 870–873.

Huang, J., Ding, F. and Yakobson, B. (2008), 'Dislocation Dynamics in Multiwalled Carbon Nanotubes at High Temperatures', *Physical Review Letters* **100**(3).

Huang, M., Mao, S., Feick, H., Yan, H., Wu, Y., Kind, H., Weber, E., Russo, R. and Yang, P. (2001), 'Room-Temperature Ultraviolet Nanowire Nanolasers', *Science* **292**(5523), 1897–1899.

Johansson, J., Karlsson, L., Svensson, C., Martensson, T., Wacaser, B., Deppert, K., Samuelson, L. and Seifert, W. (2006), 'Structural Properties of (111)B-Oriented III-V Nanowires', *Nature Materials* **5**(7), 574–580.

Joyce, H., Gao, Q., Tan, H., Jagadish, C., Kim, Y., Zhang, X., Guo, Y. and Zou, J. (2007), 'Twin-Free Uniform Epitaxial GaAs Nanowires Grown by a Two-Temperature Process', *Nano Letters* **7**(4), 921–926.

Kang, K. and Cai, W. (2007), 'Brittle and Ductile Fracture of Semiconductor Nanowires - Molecular Dynamics Simulations', *Philosophical Magazine* **87**(14-15), 2169–2189.

Kganyago, K. R. and Ngoepe, P. E. (2003), 'Structural and electronic properties of lithium intercalated graphite lic6', *Physical Review B* **68**(20), 205111.

Kim, H., Han, B., Choo, J. and Cho, J. (2008), 'Three-Dimensional Porous Silicon Particles for Use in High-Performance Lithium Secondary Batteries', *Angewandte Chemie-International Edition* **47**(52), 10151–10154.

Kim, K., Zhao, Y., Jang, H., Lee, S., Kim, J., Kim, K., Ahn, J., Kim, P., Choi, J. and Hong, B. (2009), 'Large-Scale Pattern Growth of Graphene Films for Stretchable Transparent Electrodes', *Nature* **457**(7230), 706–710.

Kresse, G. and Furthmuller, J. (1996), 'Efficient Iterative Schemes for ab initio Total-Energy Calculations Using a Plane-Wave Basis Set', *Physical Review B* **54**(16), 11169–11186.

Kresse, G. and Joubert, D. (1999), 'From Ultrasoft Pseudopotentials to the Projector Augmented-Wave Method', *Physical Review B* **59**(3), 1758–1775.

Lavington, S. H. (1998), *A History of Manchester Computers - 2nd Ed.*, Swindon: The British Computer Society.

Lee, C., Wei, X., Kysar, J. and Hone, J. (2008), 'Measurement of the Elastic Properties and Intrinsic Strength of Monolayer Graphene', *Science* **321**(5887), 385–388.

Levendorf, M., Ruiz-Vargas, C., Garg, S. and Park, J. (2009), 'Transfer-Free Batch Fabrication of Single Layer Graphene Transistors', *Nano Letters* **9**(12), 4479–4483.

Li, X., Cai, W., An, J., Kim, S., Nah, J., Yang, D., Piner, R., Velamakanni, A., Jung, I., Tutuc, E., Banerjee, S., Colombo, L. and Ruoff, R. (2009), 'Large-Area Synthesis of High-Quality and Uniform Graphene Films on Copper Foils', *Science* **324**(5932), 1312–1314.

Li, Z., Dharap, P., Sharma, P., Nagarajaiah, S. and Yakobson, B. (2005), 'Continuum Field Model of Defect Formation in Carbon Nanotubes', *Journal of Applied Physics* **97**(7).

Liu, P., Wang, J., Hicks-Garner, J., Sherman, E., Soukiazian, S., Verbrugge, M., Tataria, H., Musser, J. and Finamore, P. (2010), 'Aging mechanisms of lifepo4 batteries deduced by electrochemical and structural analyses', *Journal of the Electrochemical Society* **157**(4), A499–A507.

Lu, Q. and Bhattacharya, B. (2005), 'Effect of Randomly Occurring Stone-Wales Defects on Mechanical Properties of Carbon Nanotubes using Atomistic Simulation', *Nanotechnology* **16**(4), 555–566.

Magasinski, A., Dixon, P., Hertzberg, B., Kvit, A., Ayala, J. and Yushin, G. (2010), 'High-Performance Lithium-Ion Anodes Using a Hierarchical Bottom-Up Approach', *Nature Materials* **9**(4), 353–358.

Makeev, M., Srivastava, D. and Menon, M. (2006), 'Silicon Carbide Nanowires Under External Loads: An Atomistic Simulation Study', *Physical Review B* **74**(16).

Malola, S., Hakkinen, H. and Koskinen, P. (2010), 'Structural, Chemical and Dynamical Trends in Graphene Grain Boundaries', *Physical Review B* **81**(16), 165447.

McDowell, M. T., Lee, S. W., Ryu, I., Wu, H., Nix, W. D., Choi, J. W. and Cui, Y. (2011), 'Novel Size and Surface Oxide Effects in Silicon Nanowires as Lithium Battery Anodes', *Nano Letters* **11**(9), 4018–4025.

Needleman, A. (1987), 'A continuum model for void nucleation by inclusion debonding', *Journal of Applied Mechanics-Transactions of the Asme* **54**(3), 525–531.

Ng, H., Han, J., Yamada, T., Nguyen, P., Chen, Y. and Meyyappan, M. (2004),

'Single Crystal Nanowire Vertical Surround-Gate Field-Effect Transistor', *Nano Letters* **4**(7), 1247–1252.

Nishidate, Y. and Nikishkov, G. (2007), 'Effect of Thickness on the Self-Positioning of Nanostructures', *Journal of Applied Physcs* **102**(8), 083501.

Obrovac, M. and Christensen, L. (2004), 'Structural Changes in Silicon Anodes During Lithium Insertion/Extraction', *Electrochemical and Solid State Letters* **7**(5), A93–A96.

Obrovac, M. N. and Krause, L. J. (2007), 'Reversible Cycling of Crystalline Silicon Powder', *Journal of the Electrochemical Society* **154**(2), A103–A108.

Osing, J. and Shvets, I. (1998), 'Bulk Defects in Graphite Observed With a Scanning Tunnelling Microscope', *Surface Science* **417**(1), 145–150.

Patolsky, F., Zheng, G. and Lieber, C. (2006), 'Fabrication of Silicon Nanowire Devices for Ultrasensitive, Label-Free, Real-Time Detection of Biological and Chemical Species', *Nature Protocols* **1**(4), 1711–1724.

Pei, Q., Zhang, Y. and Shenoy, V. (2010), 'A Molecular Dynamics Study of the Mechanical Properties of Hydrogen Functionalized Graphene', *Carbon* **48**(3), 898–904.

Perdew, J., Burke, K. and Ernzerhof, M. (1996), 'Generalized Gradient Approximation Made Simple', *Physical Review Letters* **77**(18), 3865–3868.

Persson, K., Sethuraman, V. A., Hardwick, L. J., Hinuma, Y., Meng, Y. S., van der Ven, A., Srinivasan, V., Kostecki, R. and Ceder, G. (2010), 'Lithium diffusion in graphitic carbon', *Journal of Physical Chemistry Letters* **1**(8), 1176–1180.

Pettersson, H., Tragardh, J., Persson, A., Landin, L., Hessman, D. and Samuelson, L. (2006), 'Infrared Photodetectors in Heterostructure Nanowires', *Nano Letters* **6**(2), 229–232.

Plimpton, S. (1995), 'Fast Parallel Algorithms for Short-Range Molecular-Dynamics', *Journal of Computational Physics* **117**(1), 1–19. http://lammps.sandia.gov

Pong, W., Bendall, J. and Durkan, C. (2007), 'Observation and Investigation of Graphite Superlattice Boundaries by Scanning Tunneling Microscopy', *Surface Science* **601**(2), 498–509.

Ross, F. (2009), 'Nanowires Bringing Order to Twin-Plane Defects', *Nature Nanotechnology* **4**(1), 17–18.

Ryu, I., Choi, J. W., Cui, Y. and Nix, W. D. (2011), 'Size-Dependent Fracture of Si Nanowire Battery Anodes', *Journal of the Mechanics and Physics of Solids* **59**(9), 1717–1730.

Sethuraman, V. A., Chon, M. J., Shimshak, M., Srinivasan, V. and Guduru, P. R. (2010), 'In Situ Measurements of Stress Evolution in Silicon Thin Films During Electrochemical Lithiation and Delithiation', *Journal of Power Sources* **195**(15), 5062–5066.

Shenoy, V. B., Johari, P. and Qi, Y. (2010), 'Elastic Softening of Amorphous and Crystalline Li-Si Phases with Increasing Li Concentration: A first-Principles Study', *Journal of Power Sources* **195**(19), 6825–6830.

Simonis, P., Goffaux, C., Thiry, P., Biro, L., Lambin, P. and Meunier, V. (2002), 'STM Study of a Grain Boundary in Graphite', *Surface Science* **511**(1-3), 319–322.

Smith, W. F. (2004), *Foundations of Materials Science and Engineering*, McGraw Hill.

Song, T., Xia, J., Lee, J. H., Lee, D. H., Kwon, M. S., Choi, J. M., Wu, J., Doo, S. K., Chang, H., Il Park, W., Zang, D. S., Kim, H., Huang, Y., Hwang, K. C., Rogers, J. A. and Paik, U. (2010), 'Arrays of Sealed Silicon Nanotubes As Anodes for Lithium Ion Batteries', *Nano Letters* **10**(5), 1710–1716.

Stuart, S., Tutein, A. and Harrison, J. (2000), 'A Reactive Potential for Hydrocarbons with Intermolecular Interactions', *Journal of Chemical Physics* **112**(14), 6472–6486.

Tersoff, J. (1989), 'Modeling solid-state chemistry: Interatomic potentials for multicomponent systems', *Physical Review B* **39**(8), 5566–5568.

Thelander, C., Nilsson, H., Jensen, L. and Samuelson, L. (2005), 'Nanowire Single-Electron Memory', *Nano Letters* **5**(4), 635–638.

Verheijen, M., Algra, R., Borgstrom, M., Immink, G., Sourty, E., van Enckevort, W., Vlieg, E. and Bakkers, E. (2007), 'Three-Dimensional Morphology of GaP-GaAs Nanowires Revealed by Transmission Electron Microscopy Tomography', *Nano Letters* **7**(10), 3051–3055.

Wen, B., Sader, J. and Boland, J. (2008), 'Mechanical Properties of ZnO Nanowires', *Physical Review Letters* **101**(17).

Williams, M. (1952), 'Stress Singularities Resulting from Various Boundary Conditions in Angular Corners of Plates in Extension', *Journal of Applied Mechanics* **19**, 526–528.

Wong, H., Durkan, C. and Chandrasekhar, N. (2009), 'Tailoring the Local Interaction between Graphene Layers in Graphite at the Atomic Scale and Above Using Scanning Tunneling Microscopy', *ACS Nano* **3**(11), 3455–3462.

Woodford, W. H., Chiang, Y. M. and Carter, W. C. (2010), 'Electrochemical shock

of intercalation electrodes: A fracture mechanics analysis', *Journal of the Electrochemical Society* **157**(10), A1052–A1059.

Xiao, J., Staniszewski, J. and Gillespie, J. (2009), 'Fracture and Progressive Failure of Defective Graphene Sheets and Carbon Nanotubes', *Composite Structures* **88**(4), 602–609.

Xiao, J., Staniszewski, J. and Gillespie, J. (2010), 'Tensile Behaviors of Graphene Sheets and Carbon Nanotubes with Multiple Stone-Wales Defects', *Materials Science and Engineering A - Structural Materials Properties Microstructure and Processing* **527**(3), 715–723.

Yazyev, O. and Louie, S. (2010), 'Topological Defects in Graphene: Dislocations and Grain Boundaries', *Physical Review B* **81**(19), 195420.

Yu, Q., Lian, J., Siriponglert, S., Li, H., Chen, Y. and Pei, S. (2008), 'Graphene Segregated on Ni Surfaces and Transferred to Insulators', *Applied Physics Letters* **93**(11).

Zhang, H. L., Li, F., Liu, C., Tan, J. and Cheng, H. M. (2005), 'New insight into the solid electrolyte interphase with use of a focused ion beam', *Journal of Physical Chemistry B* **109**(47), 22205–22211.

Zhang, S., Mielke, S., Khare, R., Troya, D., Ruoff, R., Schatz, G. and Belytschko, T. (2005), 'Mechanics of Defects in Carbon Nanotubes: Atomistic and Multiscale Simulations', *Physical Review B* **71**(11).

Zhang, X., Jiao, K., Sharma, P. and Yakobson, B. (2006), 'An Atomistic and Non-Classical Continuum Field Theoretic Perspective of Elastic Interactions Between Defects (Force Dipoles) of Various Symmetries and Application to Graphene', *Journal of the Mechanics and Physics of Solids* **54**(11), 2304–2329.

Zhang, X., Sastry, A. and Shyy, W. (2008), 'Intercalation-Induced Stress and Heat Generation Within Single Lithium-Ion Battery Cathode Particles', *Journal of the Electrochemical Society* **155**(7), A542–A552.

Zhang, X., Shyy, W. and Sastry, A. (2007), 'Numerical Simulation of Intercalation-Induced Stress in Li-ion Battery Electrode Particles', *Journal of the Electrochemical Society* **154**(10), A910–A916.

Zhang, Y. and Huang, H. (2009), 'Do Twin Boundaries Always Strengthen Metal Nanowires?', *Nanoscale Research Letters* **4**(1), 34–38.

Zhang, Y., Shim, H. and Huang, H. (2008), 'Size Dependence of Twin Formation Energy in Cubic SiC at the Nanoscale', *Applied Physics Letters* **92**(26), 261908.

Zhao, K., Pharr, M., Vlassak, J. J. and Suo, Z. (2010), 'Fracture of Electrodes in Lithium-Ion Batteries Caused by Fast Charging', *Journal of Applied Physics* **108**(7), 073517.

Zhu, Y., Xu, F., Qin, Q., Fung, W. and Lu, W. (2009), 'Mechanical Properties of Vapor-Liquid-Solid Synthesized Silicon Nanowires', *Nano Letters* **9**(11), 3934–3939.